University of Southampton

Faculty of Environmental and Life Sciences

Ocean and Earth Science

A statistical funnel-based approach to assess spatial contributions to uncertainty in organic carbon flux attenuation.

by

Benoit Henri Guillaume Espinola

ORCID ID 0000-0003-2412-9645

Thesis for the degree of Master of Philosophy

June 2022

University of Southampton

Abstract

Faculty of **Environmental and Life Sciences**

Ocean and Earth Science

Master of Philosophy

A statistical funnel-based approach to assess spatial contributions to uncertainty in organic carbon flux attenuation.

by

Benoit Henri Guillaume Espinola

The biological carbon pump (BCP) is one of the atmospheric CO_2 pathways into the ocean and plays a major role in climate regulation. Primary production in the ocean uptakes CO_2 to produce organic matter, which enters the food chain and undergoes transformations to become particulate organic carbon (POC). The POC sinks transporting carbon into the ocean, creating a POC flux. As it sinks, POC gets respired and releases CO_2 back into the environment, attenuating the flux. The deeper this happens, the longer the released CO_2 stays away from the atmosphere. Sediment traps and the Martin's curve, a statistical fit of a power law, are commonly used to describe this flux attenuation with depth. The use of sediment traps assumes the flux captured by traps deployed simultaneously at different depths comes from the same region. The source of the flux plays a key role in understanding observations of the BCP. Unusual/unexpected flux profiles might be caused by variability in fields on the ocean's surface. To know the source region of the flux, one must find its "statistical funnel". A particle backtracking approach can be used to achieve this; however, the currently used approach does not account for uncertainties in ocean currents. Additionally, the existing method for the statistical funnel backtracks particles until they reach the ocean's surface. This is not necessarily accurate as the surface layer of the ocean is well mixed. Particles in the mixed surface layer does not make sense as particles could come from any point within the mixed layer.

Here I suggest a method to calculate a statistical funnel considering uncertainties in ocean currents. From this funnel study I also suggest a method to estimate the contributions of spatial variability in the traps' catchment areas to the uncertainty in Martin's "b-value" (which represents the flux attenuation). The method also suggests a spatially adjusted b-value, which considers each trap's catchment area. Finally, I present a case study that found that spatial variability can contribute up to 25% in the uncertainty in a b-value obtained from POC flux observation.

Table of Contents

Table of Contents ..... **i**

Table of Tables ..... **iii**

Table of Figures ..... **v**

Research Thesis: Declaration of Authorship ..... **ix**

Acknowledgements ..... **xi**

Definitions and Abbreviations ..... **xiii**

Introduction **15**

Ocean's CO_2 intake pathways 15

The biological carbon pump 15

Particulate organic carbon sinking 17

Martin's curve and the b-value 18

The statistical funnel 19

Methods 22

Field campaign 22

Fitting Martin's b-value 24

Particle backtracking 24

Backtracking with Monte-Carlo method 25

Quantifying the contribution of spatial variability to uncertainties in b 26

Top:funnel ratio 26

Spatially adjusted b 28

Data sources 29

Results 30

Trap trajectories 30

POC flux depth profile and b-value estimate 32

Distribution of the distances between the sampling location and each point in the statistical funnel 33

Density plots 34

Top:funnel–ratio 35

Distribution of spatially adjusted b-values 37

Discussion 38

Limitations of the approach 41

Limitations of the case study 42

Implications of the case study results 43

Conclusions 44

Future work 44

Glossary of Terms 47

List of References 49

Table of Tables

Table 1 Location of the traps at their deployment and emerging positions and the depths at which they stabilised. 24

Table 2 summary of the top:funnel ratio bias estimate when assuming the flux sinks straight down. A plus sign means the value overestimated, a minus sign means the value is underestimated, and an equal sign suggests that for this case, spatial processes did not affect the estimate (note that this is only valid for a single point, for a region, all the top:funnel ratios should be equal to 1 so that the region is free from spatial effects). 27

Table 3 Comparing top:funnel ratios of two traps (denoted A and B). This comparation is only valid if the value over the traps are the same. 28

Table of Figures

Figure 1 The biological carbon pump: primary production captures atmospheric CO_2 to produce particulate organic carbon (POC). The sinking POC creates a flux that is respired as it sinks, releasing CO_2 back into the environment. The deeper the CO_2 released, the longer it is expected that the released CO_2 returns to the atmosphere. Figure adapted from Herndl and Reinthaler (2013). 16

Figure 2 The biological carbon pump's facets: transportation pathways of CO_2 into the ocean. Adapted from Boyd et al. (2019). 17

Figure 3 Martin's curve using VERTEX flux data, adapted from Martin et al. (1987). .. 18

Figure 4 Statistical funnel obtained by backtracking sinking particles captured by sediment traps in the Sargasso Sea, adapted from Siegel and Deuser (1997). The circles correspond to the distances containing 30%, 60%, 80% 90% and 95% (respectively from the inner-most to the outer-most circles) of the particles collected by the traps according to their depth (H) and the particle sinking speed (WS). 20

Figure 5 Statistical funnel study from two COMICS I deployments using the Espinola (2018) approach. The contour lines are the outlines englobing the source region for particles sinking at 15 m day^{-1}, captured by PELAGRA traps P2, P4, P6, P7 and P9, respectively at 110 m, 90 m, 150 m, 250 m and 500 m depth. Adapted from Espinola (2018). 21

Figure 6 (Left) Weekly satellite derived chlorophyll a concentration in sea water as measured by the VIIRS sensor cantered on 22-November-2017. The red dot is the sampling station used in this analysis. (Right) Mean cup opening location (yellow triangle) with satellite chlorophyll-a observations from the "VIIRS-SNPP Standard Mapped" product on 11 November 2017. Note the log-scale for the chlorophyll axis. Vectors on the right pane show the surface ocean velocity with a maximum magnitude of 33.9 cm s^{-1}. 23

Figure 7 Linearly interpolated trajectories of the PELAGRA sediment traps deployed during COMICS I near P3B. The black diamonds represent the interpolated position when the collection cups opened (cup 1 of each PELAGRA sediment

trap). The white triangle and the inverted triangle are the position where the 88 m and 92 traps emerged respectively 31

Figure 8 Red circles are the POC flux measured in the deployment 6 series, cup 1. Black dots were used to fit Martin's curve and estimate b (0.31 ± 0.50, with an adjusted R^2 of 0.69). Note that the results from the two shallow-most traps were combined and the mean POC was used to fit Martin's curve. 32

Figure 9 Horizontal distances of each point in the statistical funnel (position of the intercept of the particle's path with the base of the mixed layer) to the trap cup opening position at the time of capture for traps deployed to 90 m, 136 m, 240 m, and 520 m depth. The blue rectangles correspond to the interquartile range of the distribution of distances with respect to depth. The red line in the boxes corresponds to the median of the distribution of distances with respect to depth. The black bars in the extremity of the whiskers correspond to the statistical minimum and maximum values in the distribution of distances with respect to depths excluding statistical outliers. The red crosses correspond to statistical outliers. 33

Figure 10 Probable POC flux source regions. Panels (a-d) present the results for the trap at 90 m, 136 m, 240 m and 520 m depth respectively. The black line is the envelope enclosing all the points in the particle backtracking results (classic approach of a statistical funnel). The shaded squares represent the probability of that area to be the source region; the figures inside these squares are the probability that square is the source of the particles arriving at the trap. 34

Figure 11 Histogram of the distribution of top:funnel chlorophyll ratios. Panels a-d present the results for the trap at 90 m, 136 m, 240 m, and 520 m depth. The blue dotted line represents a perfect match in chlorophyll concentration above the trap and at the source funnel. Note the log-scale in both axes. 36

Figure 12 Probability distribution of spatially adjusted b-values (black curve). The mean and median of the distribution were 0.27 (red line) and the measured b-value was 0.31 (blue line). The 95 % interval centred on the mean of the distribution was [0.11; 0.38]. 37

Figure 13 Summary figure presenting the approach of the analysis comparing the two deepest traps (denoted c and d). This composite figure is an adaptation of Figure

6, Figure 8, Figure 10, and Figure 11. Blue lines correspond to the trap c and red corresponds to trap d. 39

Figure 14 Summary of the method. The blue path is the workflow that is currently used by the community. The green path is my suggested method to complement the current workflow. Parallelograms represent loading/saving data, rectangles are processes, circles are in page references and balloons are graphical outputs. Arrows represent processes inputs/outputs. They also correspond to the processes flow. The white circles correspond to the starting and ending point of the flowchart. 40

Research Thesis: Declaration of Authorship

Print name: Benoit Henri Guillaume Espinola

Title of thesis: A statistical funnel-based approach to assess spatial contributions to uncertainty in organic carbon flux attenuation.

I declare that this thesis and the work presented in it are my own and has been generated by me as the result of my own original research.

I confirm that:

1. This work was done wholly or mainly while in candidature for a research degree at this University;
2. Where any part of this thesis has previously been submitted for a degree or any other qualification at this University or any other institution, this has been clearly stated;
3. Where I have consulted the published work of others, this is always clearly attributed;
4. Where I have quoted from the work of others, the source is always given. With the exception of such quotations, this thesis is entirely my own work;
5. I have acknowledged all main sources of help;
6. Where the thesis is based on work done by myself jointly with others, I have made clear exactly what was done by others and what I have contributed myself;
7. None of this work has been published before submission.

Signature: .....Date: Wednesday, 1 June 2022

Acknowledgements

This thesis marks the end of a journey full of challenges.

I would like to thank my supervisors, Dr Stephanie Henson, Dr Nathan Briggs, Dr Filipa Carvalho, and Dr Anna Hickman, for their support and advice throughout my M.Phil. journey. I am especially grateful for their encouragement and understanding at all times. Additionally, thanks to my panel chair, Prof Dr Tom Bibby, for his time and dedication.

I extend my gratitude to Dr Sari Giering, who played a key role in fostering my interest in pursuing this degree. Thanks go to: Corinne Pebody, Dr Sari Giering, and Hannah East, for their prompt help with COMICS data; Dr Eleanor Frajka-Williams for her help and comments; Dr Richard Lampitt, Dr Henry Ruhl, Dr Richard Sanders and Dr Adrian Martin for their inputs and opportunities; Dr Chelsey Baker for the help, guidance, and chats at the start of my journey.

Thanks to Kimmo Tikka, for his friendly support and opportunities; to UEA for the Ocean Glider ATSC course; MINES ParisTech for the Les Méthodes de la Géostatistique course and, in particular, Dr Nathalie Dietrich for organising the course and her help during my stay in Fontainebleau; 8th EGO Meeting and International Glider Workshop Organizing Committee, and especially Dr Andrew George (from NOAA), for the travel support and opportunity for me to participate in the 8th EGO meeting. I also acknowledge the use of the IRIDIS High Performance Computing Facility, and associated support services at the University of Southampton, in the completion of this work.

To my colleagues and friends, Dr Francisco De Melo Viríssimo, Dr B.B. Cael, Mike Buckingham, Pablo Tucco, Nathan Hubot, Sarah Cryer, Vanesa Romero, Dr Alex Loveridge, Dr Rebecca De Leij, Rachel Rayne, and Dr Ali Almosawy, thank you for your support and kindness, on and off campus.

Special thanks to my wife, Anu Suonpää-Espinola (+baby boy #2), and our son Elias Espinola, for their unconditional support and patience during my journey. To my parents, Arlette Espinola and Humberto Espinola, warmest eternal gratitude. Without the support of my close family, I would not have been able to go through this journey.

Finally, I would like to thank my friends Dr Julien Mineraud, Dr Marko Kallio, Capt. Nicolas Godet, Márcia Costa Ferreira, Pete Cato, Estela Riehl, Dr Salomé Espinola, Ricardo Espinola, Gabriel d'Oliveira, and Sally Thompson. You all contributed in your own ways.

I dedicate this thesis to the loving memory of my mother, Arlette Espinola.

To all who contributed in their own way: Thank you, Merci, Obrigado, Kiitos, Tack, Tak, Gracias, Danke, Gràcies.

Definitions and Abbreviations

BCP..... Biological carbon pump: atmospheric carbon removal by the ocean's biology.

DIC..... Dissolved inorganic carbon: aqueous inorganic carbon in the ocean

NOC..... National Oceanography Centre

PELAGRA ..... Particle Export measurement using a Lagrangian trap: a drifting autonomous sediment trap used to collect and/or observe particulate organic carbon flux at a target depth and time.

PAP..... Porcupine Abyssal Plain: long-term study site located in the Northeast Atlantic Ocean at 49.0°N 016.5°W with a depth of 4850 m.

POC ..... Particulate organic carbon: fraction of the organic carbon with a size ranging from 53 μm to 2 mm.

Introduction

Ocean's CO_2 intake pathways

The ocean has taken up a quarter of the anthropogenic CO_2 emissions since the beginning of the industrial revolution (Friedlingstein et al. 2019). This anthropogenic CO_2 uptake varies both spatially and temporally on seasonal and interannual scales (Gruber et al. 2019; Landschützer et al. 2019; Roobaert et al. 2019; Wanninkhof et al. 2013; Watson et al. 2009).

CO_2 is continuously exchanged between the atmosphere and the ocean. This continuous exchange is driven by atmospheric and oceanic CO_2 concentrations and by the turbulence in the ocean-atmosphere interface (Smith et al. 2018; Woolf et al. 2016). In sea water, gaseous CO_2 is submitted to a series of chemical reactions, which ultimately results in aqueous CO_2 being stored in oceanic waters; this is known as the solubility pump (Laruelle et al. 2014; Roobaert et al. 2019; Shadwick et al. 2010). The carbonate system is composed of aqueous CO_2, carbonate, bicarbonate, and carbonic acid (Humphreys et al. 2022). Adding these together I obtain the total inorganic carbon, also known as dissolved inorganic carbon (DIC). Atmospheric CO_2 exchanges are not the only sources of DIC; riverine and coastal inputs also contribute to seawater DIC (Tranvik et al. 2009). Respiration processes in the ocean are another source of DIC, and these will be further discussed in the next section.

The biological carbon pump

The biological carbon pump (BCP) is important in maintaining the air-sea balance of CO_2 (Henson et al. 2011; Kwon et al. 2009). Without the BCP, atmospheric CO_2 concentrations would be 50% higher than currently (Kwon et al. 2009; Parekh et al. 2006), i.e., an additional 200 ppm of CO_2. There is a pressing need to study the BCP and the sources of uncertainty, as it could be impacted by climate change (Henson et al. 2022). Additionally, the BCP is the main mechanism that supplies mesopelagic and benthic ecosystems with food, in the form of particulate organic carbon (POC) (Fowler and Knauer 1986). The BCP therefore also plays a major role in deep-sea biogeochemistry and ecology.

The BCP is a collection of processes which starts with photosynthesis, where phytoplankton uses light and nutrients to bind CO_2 and produce organic compounds (Boyd et al. 2019; Giering and Humphreys 2017). These compounds are later used by the organism for growth.

Marine primary production is performed by the ensemble of autotrophic organisms that take in environmental inorganic carbon (either atmospheric or dissolved) to produce organic carbon. In the ocean, there are two pathways for primary production: chemosynthesis (which uses chemical energy to produce organic carbon) and photosynthesis (which uses radiative energy to produce organic carbon). The earlier is mainly found in deep sea systems such as hydrothermal vents. The latter is dominant across the ocean and is found in the euphotic zone, the layer of the ocean in which sunlight can penetrate with enough intensity to ensure photosynthesis by phytoplankton.

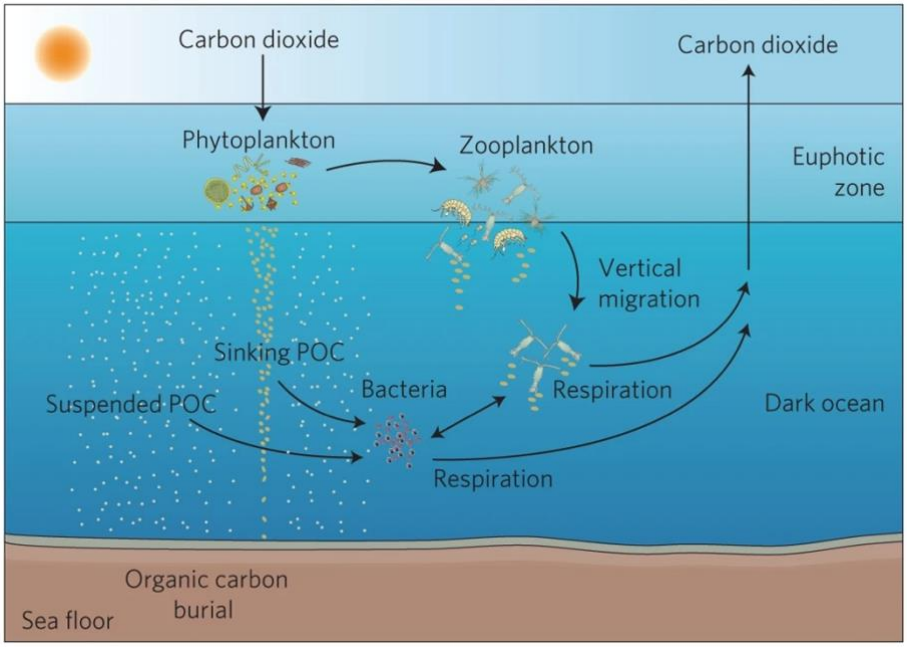

Figure 1 The biological carbon pump: primary production captures atmospheric CO_2 to produce particulate organic carbon (POC). The sinking POC creates a flux that is respired as it sinks, releasing CO_2 back into the environment. The deeper the CO_2 released, the longer it is expected that the released CO_2 returns to the atmosphere. Figure adapted from Herndl and Reinthaler (2013).

The biological carbon pump is the collection of processes where carbon fixed by the primary production is transported into the ocean's interior. In the ocean's surface layer, organic matter is continually produced and recycled (see Figure 1) (Giering and Humphreys 2017; Herndl and Reinthaler 2013). The growth and multiplication of phytoplankton is limited by the component which runs out first, this is known as the limiting factor. In the euphotic zone, this can be driven by a macronutrient, such as nitrogen or phosphorus forms, or by a micronutrient, such as iron. The availability of nutrients, varies spatially, defining biogeochemical regions, introducing special variability to the BCP. Sunlight can be a limiting factor, increasingly significant as latitudes are higher. In high latitudes, during the winter, the incoming radiation is too weak to sustain phytoplankton growth and multiplication. This results to yearly phytoplankton bloom episodes.

Organic carbon produced by primary production enters the food web to be further transformed, either to other forms of organic carbon or into forms of inorganic carbon. Respiration is one of the processes in which organic carbon is transformed into CO_2 and released in the environment. Only a fraction of the organic carbon is transported into the ocean.

Particulate organic carbon sinking

There are many carbon transportation pathways, among which are the migration pump, the eddy subduction pump, and the gravitational biological pump (Boyd et al. 2019) (see Figure 2). The gravitational biological pump, i.e., particles containing organic carbon sinking with the sole effect of gravity, is believed to be the main transportation pathway for organic carbon into the ocean. In this study, I focus on the gravitational pump which creates a downwards POC flux.

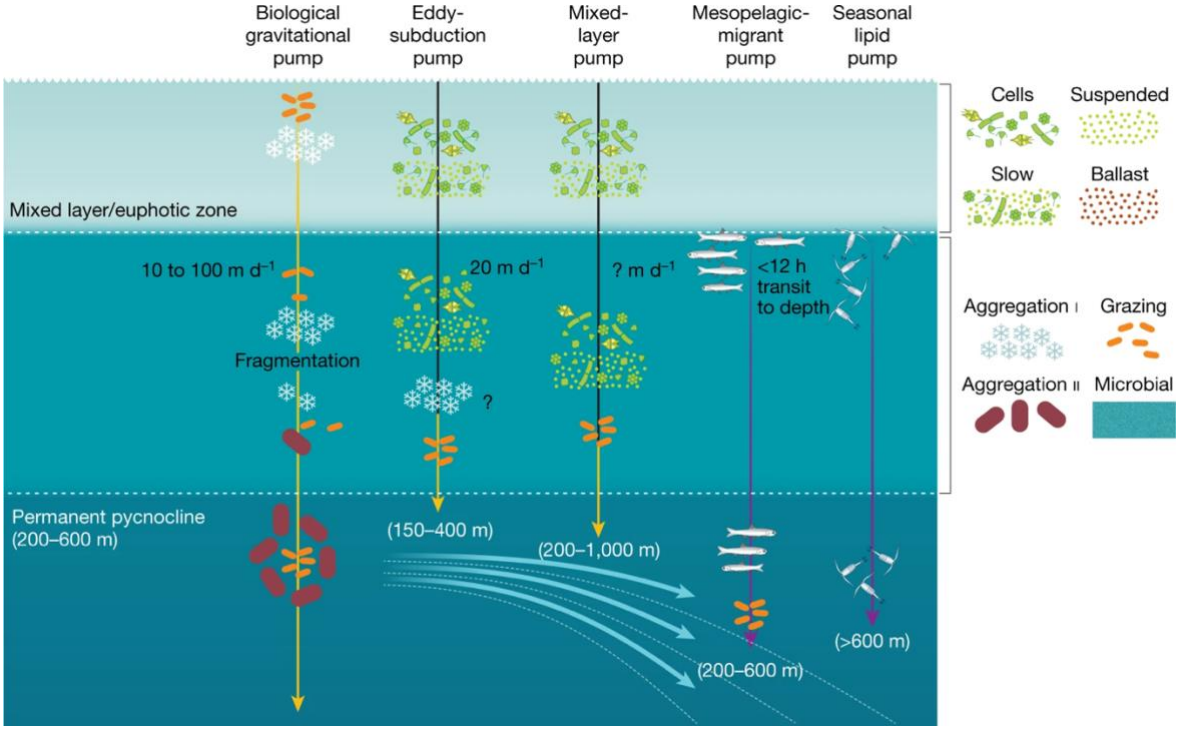

Figure 2 The biological carbon pump's facets: transportation pathways of CO_2 into the ocean. Adapted from Boyd et al. (2019).

A particle containing organic carbon sinks with a certain settling speed, which depends on the particle's density but also its three-dimensional shape. As POC sinks, particles undergo a series of transformations, among which are aggregation, repackaging, disaggregation, and respiration (Briggs et al. 2020; Buesseler and Boyd 2009; Burd and Jackson 2009; Cavan et al. 2017; Lampitt et al. 1990; Robinson et al. 2010). A particle's density can also be affected by chemical exchanges with the environment, for instance, salinity exchange between the surrounding water mass and

water pockets inside the particle. Temperature can also affect the particle's density by altering heat exchange between the particle and its environment. These transformations can alter the particle's shape and density, affecting their sinking speed.

POC is respired primarily by bacteria and zooplankton, releasing inorganic carbon in the form of CO_2 back into the environment. The depth at which this respiration process happens is known as the remineralization depth (Kwon et al. 2009). Typically, the deeper remineralisation occurs, the longer it takes for the released carbon to return to the atmosphere as CO_2, with time scales up to thousands of years (Giering and Humphreys 2017; Henson et al. 2011; Lampitt et al. 2008a; Passow and Carlson 2012). However, the remineralization depth needs to be deeper than the winter mixed layer for the carbon to be stored for long timescales (Giering and Humphreys 2017).

Martin's curve and the b-value

POC gets respired throughout its lifetime, including the fraction of POC that sinks. The respiration process reduces the carbon content of a particle while releasing CO_2 into the environment. The downward gravity driven POC flux is attenuated with depth due to consumption or re-working by the activity of zooplankton and bacteria.

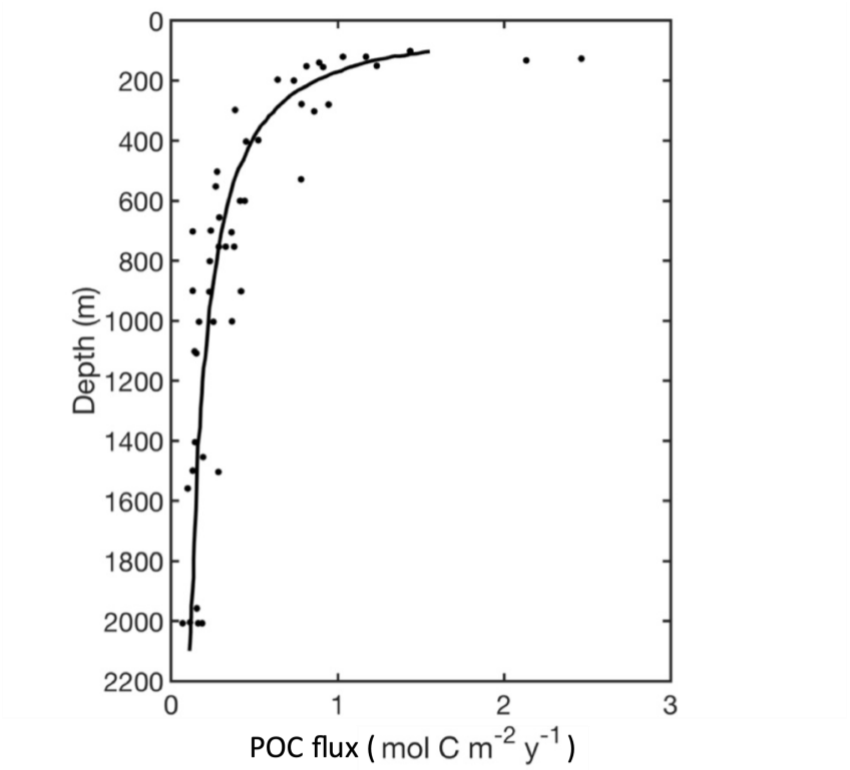

Figure 3 Martin's curve using VERTEX flux data, adapted from Martin et al. (1987).

POC flux observations can be fitted to a power law model known as Martin's curve (Martin et al. 1987), see Figure 3. There are other models that describe the POC flux attenuation with depth

(Cael and Bisson 2018), however Martin's model is still widely used because of its simplicity and goodness of fit to a wide range of observations. Equation 1 is used to obtain the Martin's curve:

$$F(Z) = F_{Z_{ref}} \cdot \left(\frac{Z}{Z_{ref}}\right)^{-b}$$

Equation 1

Where $F(Z)$ is the flux at the depth Z, $F_{Z_{ref}}$ is the flux at the reference depth Z_{ref} (here 100m) and b is the flux attenuation coefficient.

The exponent 'b' in Equation 1 describes the flux attenuation. It is an easy to apply metric for the efficiency of the biological carbon pump. A higher b (sometimes referred to as 'b-value') means the flux attenuation is stronger and implies a less efficient biological carbon pump.

The statistical funnel

It has long been recognised that particles rarely sink straight down, instead following a path in the water column determined by local advection (Deuser et al. 1988; Siegel and Deuser 1997). Additionally, particles do not necessarily come from the surface ocean and might be generated in situ, at depth (Boyd et al. 2019). The statistical funnel is defined as the surface spatial area that is likely to be the source of sinking particles observed at depth, accounting for ocean currents (Deuser et al. 1988; Siegel and Deuser 1997; Siegel et al. 1990). The region defined by the statistical funnel can be seen as the trap's "catchment area" (Siegel and Deuser 1997). A Lagrangian approach to estimate the statistical funnel, using ocean current data to recreate a particle's trajectory in the ocean backwards in time (Deuser et al. 1988; Siegel and Deuser 1997; Siegel et al. 2008; Waniek et al. 2000).

The original approach for the statistical funnel (Figure 4) has a deterministic approach where the entire vertical water column is assumed to have the same velocity as the surface currents. In practice, sub-surface currents differ from surface currents. Additionally, the original approach uses the sea surface as the intercept to define the source of the flux. The mixed layer, by definition, is well mixed, and particle concentration is assumed constant within the mixed layer. Therefore, the particle path is no longer relevant within this layer. Particles are assumed to leave the mixed layer to sink. Setting the intercept on the sea surface ignores the properties of the mixed layer and might offset the particle source.

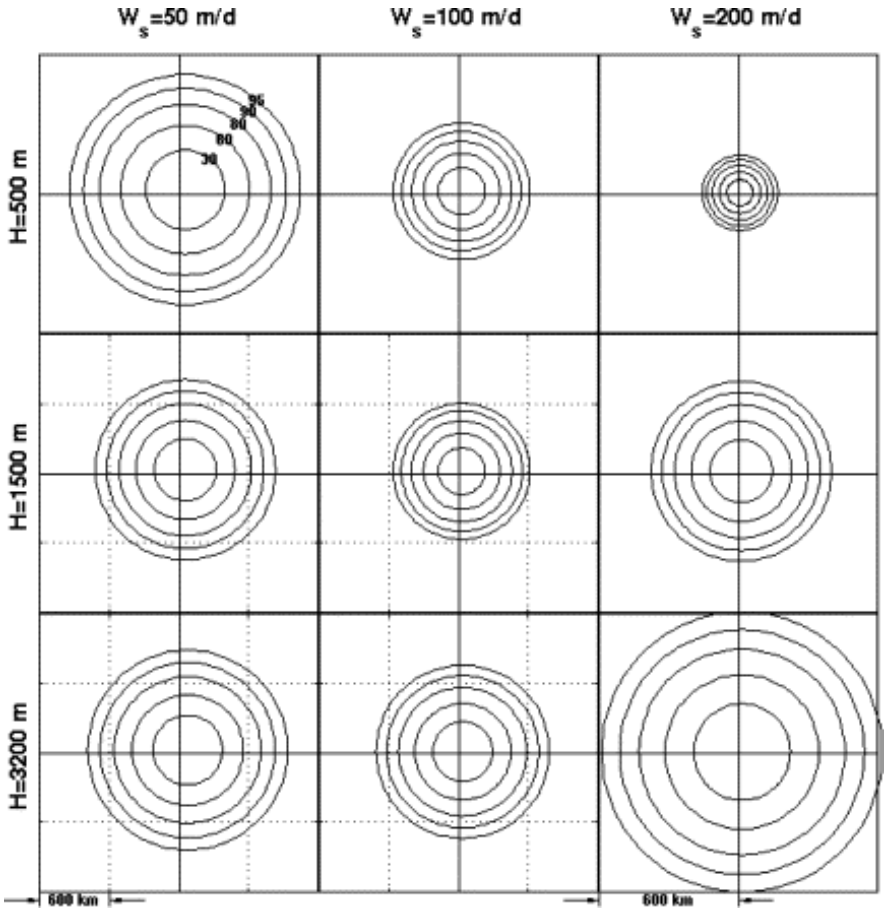

Figure 4 Statistical funnel obtained by backtracking sinking particles captured by sediment traps in the Sargasso Sea, adapted from Siegel and Deuser (1997). The circles correspond to the distances containing 30%, 60%, 80% 90% and 95% (respectively from the inner-most to the outer-most circles) of the particles collected by the traps according to their depth (H) and the particle sinking speed (W_S).

Espinola (2018) built on the top of the Siegel and Deuser (1997) approach to account uncertainties in currents. In Espinola (2018), a Monte-Carlo approach is used to estimate the source region of the POC flux captured by sediment traps (see Figure 5). Espinola (2018) uses surface currents to backtrack particles with a set sinking speed from the trap's position until they intercept the ocean's surface. Instead of a radius, Espinola (2018) outputs a set of points where each point is a possible particle source. Additionally, Espinola (2018) suggests an outline englobing most points as the source region for the POC flux. However, just like Siegel and Deuser (1997), Espinola (2018) uses surface currents throughout the water column.

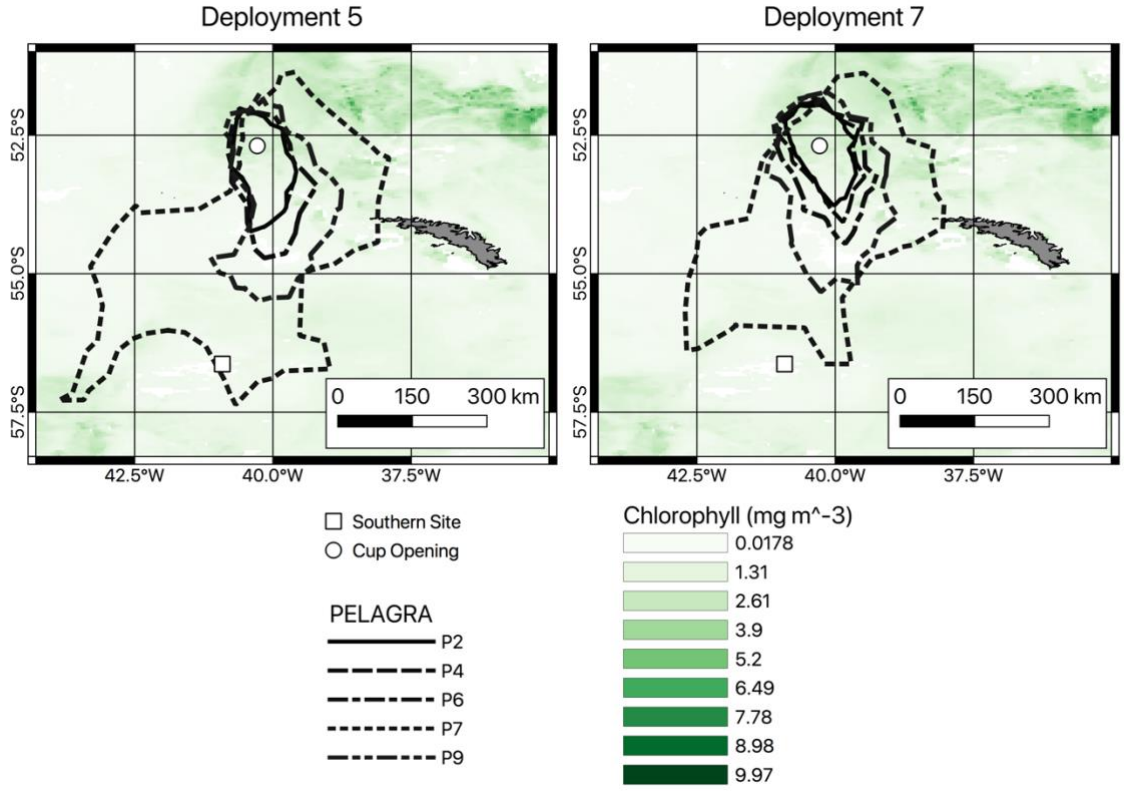

Figure 5 Statistical funnel study from two COMICS I deployments using the Espinola (2018) approach. The contour lines are the outlines englobing the source region for particles sinking at 15 m day^{-1}, captured by PELAGRA traps P2, P4, P6, P7 and P9, respectively at 110 m, 90 m, 150 m, 250 m and 500 m depth. Adapted from Espinola (2018).

Here I build upon the Espinola (2018) approach by incorporating sub-surface currents and by setting the mixed layer depth as the intercept to better define the particle source region. Additionally, instead of a cloud of points, my method outputs a rasterized probability field, where each pixel is associated with the probability that a particle with a given sinking speed reaches the trap's position. My approach also provides insights into how surface spatial variability may affect observed POC flux depth profiles and the uncertainty in the estimated b-value. The rasterized probability field can be used to better understand POC flux profile observations that differ from the expected profile, where the POC flux decreases with depth. For instance, a deep trap can measure a higher POC flux if the particle source comes from a region that has a higher POC production than shallow traps. Then, using the rasterized probability field, I normalize the POC flux observations to then obtain a distribution of spatially adjusted b-values. Finally, I use the distribution of spatially adjusted b-values to aces the contribution of spatial variability in errors when fitting Martin et al. (1987)'s b-value.

My hypothesis is that the flux comes straight down (implicit assumption made when performing parallel multi-depth sampling using sediment traps) and that the spatial processes do not contribute with POC flux profile uncertainties. My aims are to better define the source region for particles captured by sediment traps, allowing me to better understand flux profile observations. Additionally, I aim to study the relative contribution of spatial variability in the uncertainty of b-values.

Methods

Field campaign

The Controls over Ocean Mesopelagic Interior Carbon Storage (COMICS) project aims to study the processes of carbon cycling in the mesopelagic zone and how they influence ocean carbon storage (Sanders et al. 2016). The COMICS I cruise studied an area Northwest (downstream) of South Georgia, which features a naturally iron-fertilised recurrent phytoplankton bloom (Korb et al. 2008), in November and December 2017. The sampling site was near located at 52.7 °S, 48.1 °W. Neutrally buoyant, conical “Particle Export measurement using a Lagrangian trap” (PELAGRA) sediment traps (Lampitt et al. 2008b) were deployed during the cruise to obtain snapshots of the POC flux depth profile. These traps aim to sink to their respective programmed target depths and remain there for a pre-programmed length of time (typically 2-3 days), before returning to the surface for retrieval. In this study I use the POC flux data collected during the deployment series 6, where 5 PELAGRAs were deployed at 5 different target depths (see Table 1) to obtain a snapshot of the POC flux depth profile. The opening and closing of the collection cups were controlled by the PELAGRA’s internal clocks (which were synchronized between the traps prior to the deployment). The collection cups opened on 06 December 2017 at 15:00 and closed 24h later.

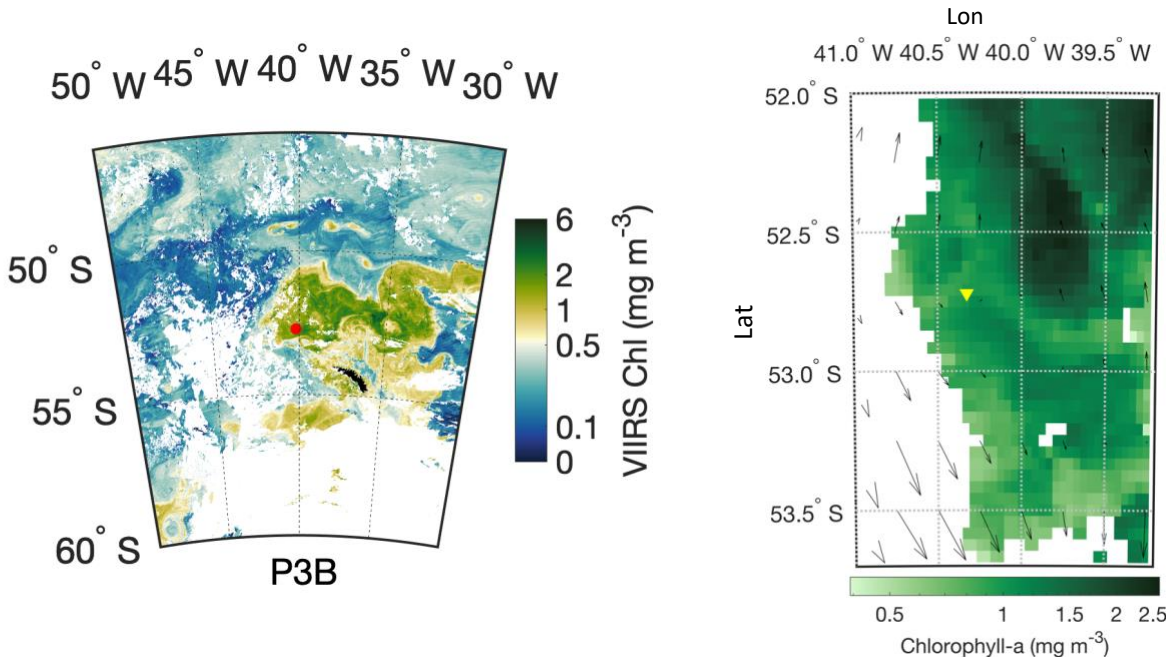

Figure 6 (Left) Weekly satellite derived chlorophyll a concentration in sea water as measured by the VIIRS sensor cantered on 22-November-2017. The red dot is the sampling station used in this analysis. (Right) Mean cup opening location (yellow triangle) with satellite chlorophyll-a observations from the "VIIRS-SNPP Standard Mapped" product on 11 November 2017. Note the log-scale for the chlorophyll axis. Vectors on the right pane show the surface ocean velocity with a maximum magnitude of 33.9 cm s^{-1}.

Figure 6 shows a snapshot of the distribution of satellite-derived chlorophyll-a concentration around the sampling region (triangle). Satellite observations of chlorophyll-a consistently show a frontal system following the currents around South Georgia, bounded by the polar front in the West. This chlorophyll plume contrasts with the predominantly low chlorophyll environment in the Southern Ocean. This chlorophyll plume is not homogenous and contains filaments and patchy areas. The sampling site was in a low chlorophyll filament with a chlorophyll concentration of 1.0 mg -m^{-3}. The sampling site contrasts with a patch, 74 km away from the study site north-east, contains the highest chlorophyll concentration 2.4 mg Chlorophyll-a m^{-3}. This contrast could be problematic for the POC flux profile if particles come from patches with a different chlorophyll concentration: e.g., a deeper trap capturing flux material coming from an area with a higher chlorophyll concentration.

The sampling site is located in an area with low magnitude currents in contrast to the surrounding region, which has strong currents including the Antarctic Circumpolar Current (Meredith 2003;

Thorpe et al. 2002). The site is thus one of low lateral advection and it might therefore be assumed that POC flux is sinking purely vertically, free of the influence of ocean currents.

Fitting Martin's b-value

I focused my analysis on cup 1 from the deployment series 6 (see Table 1for details), because the deployment was fully successful, the traps drifted within a concise region, the POC flux dataset was complete, and the POC flux profile appeared to have a good fit to a Martin's curve.

The POC flux data obtained by the PELAGRA traps were used to fit Martin's power law (Equation 1) (Martin et al. 1987). I used Matlab's (version R2020a) "fit" function to fit the data and obtain the fit coefficients ($F_{Z_{ref}}$ and b). The fit function fitted the data using a Nonlinear Least Squares which tries to find the coefficients ($F_{Z_{ref}}$ and b) by minimizing the sum of square fitting error ($min(\sum\|F(x_i) - y_i\|^2)$, where $F(x_i)$ is a nonlinear function and (x_i, y_i) are data points). The 95% confidence bounds on the coefficients associated with the fit ($F_{Z_{ref}}$ and b), noted $E_{b_{fit(flux_{POC})},95\%}$, were calculated using Matlab's (version R2020a) function "confint". The "confint" calculates the confidence bounds on coefficient by $C = b \pm t\sqrt{S}$ where b is the coefficient produced by the "fit" function, t is the inverse of the Student's t cumulative distribution function, and S is the vector composed by the diagonal elements from the estimated covariance matrix ($S = (X^T X)^{-1} s^2$, where X is the Jacobian of the fitted values with respect to the coefficients, X^T is the transpose of X, and s^2 is the mean square error)

Table 1 Location of the traps at their deployment and emerging positions and the depths at which they stabilised.

Cruise: DY086 ; Deployment Series 6			Coordinates			
	Depth (m)		in		out	
Trap code	Target	Stabilised	Latitude	Longitude	Latitude	Longitude
P7	500	520 ± 10	-52.721	-40.326	-52.688	-40.54
P9	250	240 ± 13	-52.721	-40.326	-52.693	-40.573
P6	150	136 ± 14	-52.721	-40.326	-52.75	-40.401
P4	110	88 ± 20	-52.721	-40.326	-52.75	-40.415
P2	90	92 ± 21	-52.721	-40.326	-52.752	-40.431

Particle backtracking

To estimate the flux's source region, I used a backtracking method (Deuser et al. 1988; Siegel and Deuser 1997) where the particle's previous position ($P_{(t+\Delta t)}$) is estimated based on the particle's

current position ($P_{(t)}$). The particle's displacement is estimated using the surrounding water's velocity ($U_{(P_{(t)},t)}$) with a negative time step (Δt).

$$P_{(t+\Delta t)} = P_{(t)} + U_{(P_{(t)},t)} \cdot \Delta t$$

Equation 2

This approach assumes particle have a Lagrangian-like deterministic behaviour. Since the mixed layer is, by definition, well-mixed and homogenous, particles were backtracked until they reached the base of the mixed layer.

The particle collection point was defined as the position of the trap when the first collection cup opened. This position was estimated by a linear interpolation between the last recorded position before the trap submerged and the first recorded position when the trap resurfaced. This was used as the starting point for the particle backtracking. Linearly interpolated currents were used as an estimate of the velocity at locations falling between the grid cell points.

The particle sinking speed was assumed to be 50 m day^{-1} and constant with both depth and time, for the results presented here. This sinking speed was chosen to approximate the bulk sinking speed observed in situ using sequential images mounted on a PELAGRA: 62 m day^{-1} (personal communication with Nathan Briggs – National Oceanography Centre (NOC)). The ocean's vertical velocity was assumed to be zero.

Backtracking with Monte-Carlo method

To tackle uncertainties in the current speeds, a Monte-Carlo approach was used for backtracking, where the velocity at a given position ($U_{i_{MC}}$) was estimated by a random draw from the velocity distribution in the immediate region of that position (± 2 grid points ≡ ~45 ± 11 km). The velocity distribution was assumed to be normal.

$$U_{i_{MC}} = P\left(mean(U_{i\pm2}), sd(U_{i\pm2})\right)$$

Equation 3

It then follows that:

$$P_{(t-\Delta t)} = P_{(t)} + U_{(P_{(t)},t)_{MC}} \cdot \Delta t$$

Equation 4

This Monte-Carlo approach was run 196006 times (to make sure I have a large enough number of repetitions for the rest of the method), yielding a collection of scenarios, each with one particle-source position, each with an equal likelihood. A cloud of points with possible source locations is thus obtained, i.e., the "statistical funnel". By binning the latitude and longitude of these points, the likelihood of each bin being the source region of the POC flux is obtained. The binning resolution was 1/10th of a degree.

Quantifying the contribution of spatial variability to uncertainties in b

Top:funnel ratio

To quantify error in estimates of b introduced by spatial variability, I compared the POC flux from each point of the statistical funnel with the POC flux observed in the samples collected by the trap (the latter assumes particles sink straight down). Here I use spatial variability in satellite derived chlorophyll concentration as a proxy for spatial variability in POC export flux. Although I recognise that this introduces additional uncertainty into our calculations, it is a necessary assumption as only satellite derived chlorophyll concentration provides the required spatial and temporal resolution. The implications of this assumption for our analysis are discussed in the "Implications of the case study results" section below. The ratio between the chlorophyll-a at the trap position (assuming purely vertical particle sinking) and the chlorophyll-a originating from the statistical funnel is denoted the top:funnel ratio. By doing this with all the points in the statistical funnel, I obtain a distribution of top:funnel ratios. The top:funnel ratio is calculated as follows:

$$top{:}\,funnel\ ratio\ = \frac{Chl_{top}}{Chl_{funnel}}$$

Equation 5

Where Chl_{top} is the chlorophyll directly above the trap and Chl_{funnel} is the chlorophyll at the source of the POC flux.

When assuming the flux sinks vertically, there are two scenarios where this assumption can introduce errors:

- The top to bottom scenario, is when values at depth are estimated using a surface product (i.e., the POC flux at 520 m is estimated using satellite surface chlorophyll). In this scenario, a top:funnel ratio larger than 1 implies an overestimation of the value at depth (in my example, using the satellite surface chlorophyll value and assume the flux sinks straight down would yield to a larger estimated POC flux at 520 m depth than the real

POC flux in that depth and location). On the other hand, a top:funnel ration lower than 1 implies an underestimation of the value at depth.

- The bottom to top scenario occurs when the surface value is estimated using the value observed at depth (i.e., we have POC flux observations at 520 m and would like to know the surface chlorophyll). In this scenario, a top:funnel ratio larger than 1 implies an underestimation of the surface value (in my example, using the POC flux at 520 m would give a lower surface chlorophyll than the real value). Contrarily, a top:funnel ratio that is lower than 1 implies an overestimation of the surface value. However, to establish a top:funnel ratio, the surface field needs to be known; therefore, the first scenario is more likely to occur.

A summary of the errors introduced is presented in Table 2. Note that the effects of spatial variability are not likely to affect the flux at depth if and only if all the top:funnel ratios at all depths is equal do one. If at least one top:funnel ratio differs from 1, spatial processes are likely to contribute to errors when estimating b.

Table 2 summary of the top:funnel ratio bias estimate when assuming the flux sinks straight down. A plus sign means the value overestimated, a minus sign means the value is underestimated, and an equal sign suggests that for this case, spatial processes did not affect the estimate (note that this is only valid for a single point, for a region, all the top:funnel ratios should be equal to 1 so that the region is free from spatial effects).

		Top:funnel ratio		
Scenario	Estmating	< 1	1	> 1
Top to bottom	values at depth are estimated using a surface product	-	=	+
Bottom to top	surface value is estimated using an observation at depth	+		-

Finally, because the top:funnel ratio is a continuous decreasing function for the interval $]0; \infty[$, it can be used to better understand how the source region can affect observations at depth if the top value is the same for all the traps used in the comparison. Observations at depth that derive from expected ranges (i.e., a higher POC flux in a deeper trap than a shallower trap) might be explained by the source region of the signal, and therefore reflected in the top:funnel ratios. For instance, an unusually high POC flux in a deep trap might happen if the source of that flux has larger POC concentrations. In this case, the top:funnel ratio would be larger than the top:funnel ratio of a shallower trap. However, this approach does not consider transformations in the observed values, such as flux attenuation via respiration processes.

Table 3 Comparing top:funnel ratios of two traps (denoted A and B). This comparation is only valid if the value over the traps are the same.

Top:Funnel	Trap A > Trap B	Trap A = Trap B	Trap A < Trap B
Surface value	Trap A < Trap B	Trap A = Trap B	Trap A > Trap B

A summary of the different scenarios where a top:funnel ratio is used to compare surface source values between traps who have the same surface value over the trap is presented in Table 3. Note that if traps do not share the same surface value above the traps, this comparison cannot be done. A workaround to this issue can be to calculate a new top:funnel ratio so that all the traps share the same surface value. However, this newly calculated top:funnel ratio cannot be used to perform the other analysis presented here.

Spatially adjusted b

I multiplied the top:funnel ratios by the observed POC flux and fitted a Martin's power law curve to each combination of top:funnel ratios, thus generating a probability distribution of possible b-values.

$$POC_{flux_{spatially\ adjusted}} = top{:}\,funnel\ ratio \cdot POC_{flux_{observed}}$$

Equation 6

This estimates the POC flux generated directly above the trap, removing the spatial effects found in the POC flux profile observations.

This spatially adjusted POC flux was then used to fit Martin curves to estimate b-values. By doing this with every possible combination of values, I obtain a distribution of spatially adjusted b-values. The range of the spatially adjusted b-values was then determined by finding the interval containing 95 % of the results centred by its mean so that:

$$b_{SA} = mean\left(distribution_{b_{SA}}\right) \pm E_{b_{SA},95\%}$$

Equation 7

Where b_{SA} is the spatially adjusted b-value; $mean\left(distribution_{b_{SA}}\right)$ is the mean of the distribution of fitted spatially adjusted b-values; and $E_{b_{SA},95\%}$ is the interval centred by the mean of the distribution of fitted spatially adjusted b-values such as 95% of the spatially adjusted b-values are contained in the distribution within this range. This is assumed to be the 95% confidence interval of the distribution of fitted spatially adjusted b-values.

The range $R_{interval}$ of an interval $[I_{lower}, I_{upper}]$ is the difference between its upper (I_{upper}) and lower (I_{lower}) bounds:

$$R_{interval} = I_{upper} - I_{lower}$$

Equation 8

The ratio between the range of the 95% confidence interval of the distribution of fitted spatially adjusted b-values (obtained using $E_{b_{SA},95\%}$ from Equation 7 and Equation 8) and the range of the 95% confidence bounds on the b-value associated with the fit ($R_{E_{b_{fit(flux_{POC})},95\%}}$, see the Fitting Martin's b-value section above) give us the relative contribution of the variability introduced by spatial processes in the uncertainty in the fitted b-value. This relative contribution, expressed in percent, is obtained as follow:

$$RC = \frac{R_{E_{b_{SA},95\%}}}{R_{E_{b_{fit(flux_{POC})},95\%}}}$$

Equation 9

Here, I assume a constant sinking speed and POC production exclusively occurring in the mixed layer. This assumption means that particles captured deeper will have had a longer exposure to ocean currents than particles captured at shallower depths. I also assume that the POC captured by the traps is only composed of sinking POC (part of the Biological Gravitational Pump), including the active flux; in other words, the other biological pumps stated by Boyd et al. (2019), are assumed not to contribute to the observed flux.

The source funnel of a particle is therefore dependent on its sinking speed, observation depth, mixed layer depth and ocean currents. Additionally, in a parallel, multi-depth sampling strategy, deeper traps capture older particles than shallow traps, and the particle source region might be different for traps at different depths. Therefore, uncertainty is introduced into the POC flux depth profiles both by the sampling approach itself (simultaneous capture of particles of different ages and exposure to currents) and the spatial variability of the POC field.

Data sources

For chlorophyll-a concentrations, I used daily mean, 4km resolution, L3 data from NOAA's VIIRS satellite which uses the NASA OCI Algorithm to estimate chlorophyll concentration (http://dx.doi.org/10.5067/NPP/VIIRS/L3M/CHL/2018). Because of cloud cover I could only use

the 10 November 2017 image for my analysis. This image was taken one day before the Pelagra trap deployment. The image is used as a representative chlorophyll field in the region. By using this single image for the analysis, I remove the temporal effects on the sampling.

For ocean current speeds and mixed layer depths, I used Copernicus' "global ocean 1/4° physics analysis and forecast updated daily product" assimilative model (https://resources.marine.copernicus.eu/?option=com_csw&view=details&product_id=GLOBAL_REANALYSIS_PHY_001_030). I could not validate the current data with in-situ data for my study period and region. The model is therefore being used as an example of plausible current fields in the region.

The COMICS POC flux data are described in East (2019) and were supplied to me by Sari Giering (NOC).

Results

Trap trajectories

All 5 traps were deployed in the same location; however, traps drifted during the deployment in two groups (see Figure 7). The three shallow traps drifted SE, while the two deeper traps drifted NW from the deployment location. Furthermore, the 2 deeper traps travelled further from the deployment site than the 3 shallower traps (~ 16 km vs 7 km). This suggests differences in current velocity at depths below the 136m trap compared to the currents in the upper ocean.

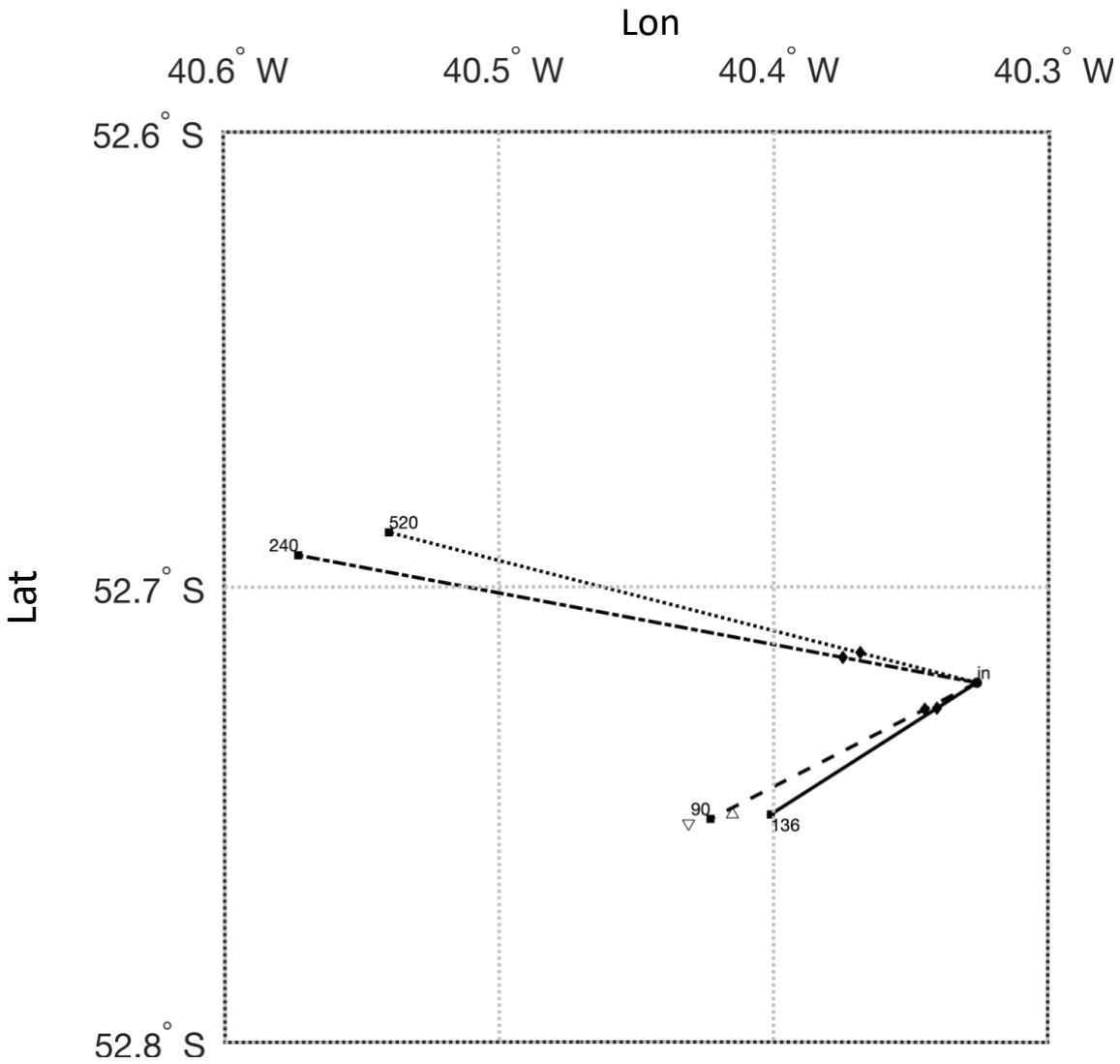

Figure 7 Linearly interpolated trajectories of the PELAGRA sediment traps deployed during COMICS I near P3B. The black diamonds represent the interpolated position when the collection cups opened (cup 1 of each PELAGRA sediment trap). The white triangle and the inverted triangle are the position where the 88 m and 92 traps emerged respectively

The estimated locations of the cups opening ranged between 1.4 km and 3.4 km away from the deployment point and the estimated distance between the traps when cups opened was between 0.1 km and 2.6 km. The cup opening and trap re-surfacing positions were close enough to each other to be within 4km, i.e., in the same or adjacent pixels in the satellite chlorophyll image. Additionally, the time scale of the traps' deployment (~2 days, cups stayed open for 24h) was short relative to the time scale of the sinking POC (from ~2 to 10.4 days, assuming a 50 m d^{-1}).

POC flux depth profile and b-value estimate

For my selected POC flux profile, the 88 and 92 m traps were considered as pseudo-replicates and their POC flux values were averaged to form a single data point at 90 m depth (see Figure 8). The deepest trap sampled a POC flux slightly larger than the 240 m trap. This is an unexpected result as POC flux is expected to decrease with depth(Martin et al. 1987). However, the difference between these two deep traps was relatively small (5 mg C m^{-2} day^{-1}) when compared to the difference between the two shallow-most traps (14 mg C m^{-2} day^{-1}).

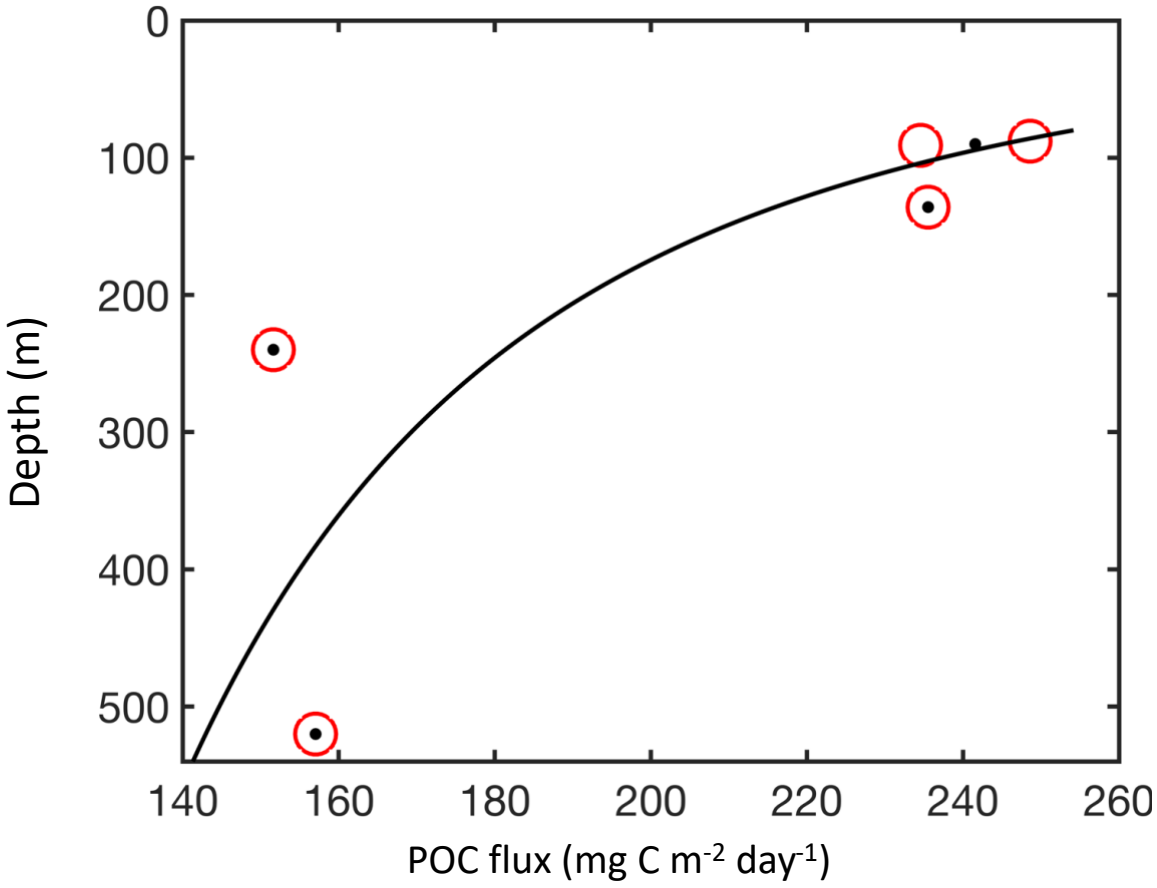

Figure 8 Red circles are the POC flux measured in the deployment 6 series, cup 1. Black dots were used to fit Martin's curve and estimate b (0.31 ± 0.50, with an adjusted R^2 of 0.69). Note that the results from the two shallow-most traps were combined and the mean POC was used to fit Martin's curve.

The b-value calculated from the POC flux profile with a 95% confidence interval was 0.31 ± 0.50 (with an adjusted R^2 of 0.69).

Distribution of the distances between the sampling location and each point in the statistical funnel

The distribution of the distances from each result of the statistical funnel to the location where the particles were collected by the traps is presented in Figure 9. Particles captured by deeper traps potentially travelled longer and more variable horizontal distances than particles captured by shallower traps. The increase in spread represents an increase in uncertainty of the POC flux source region with depth.

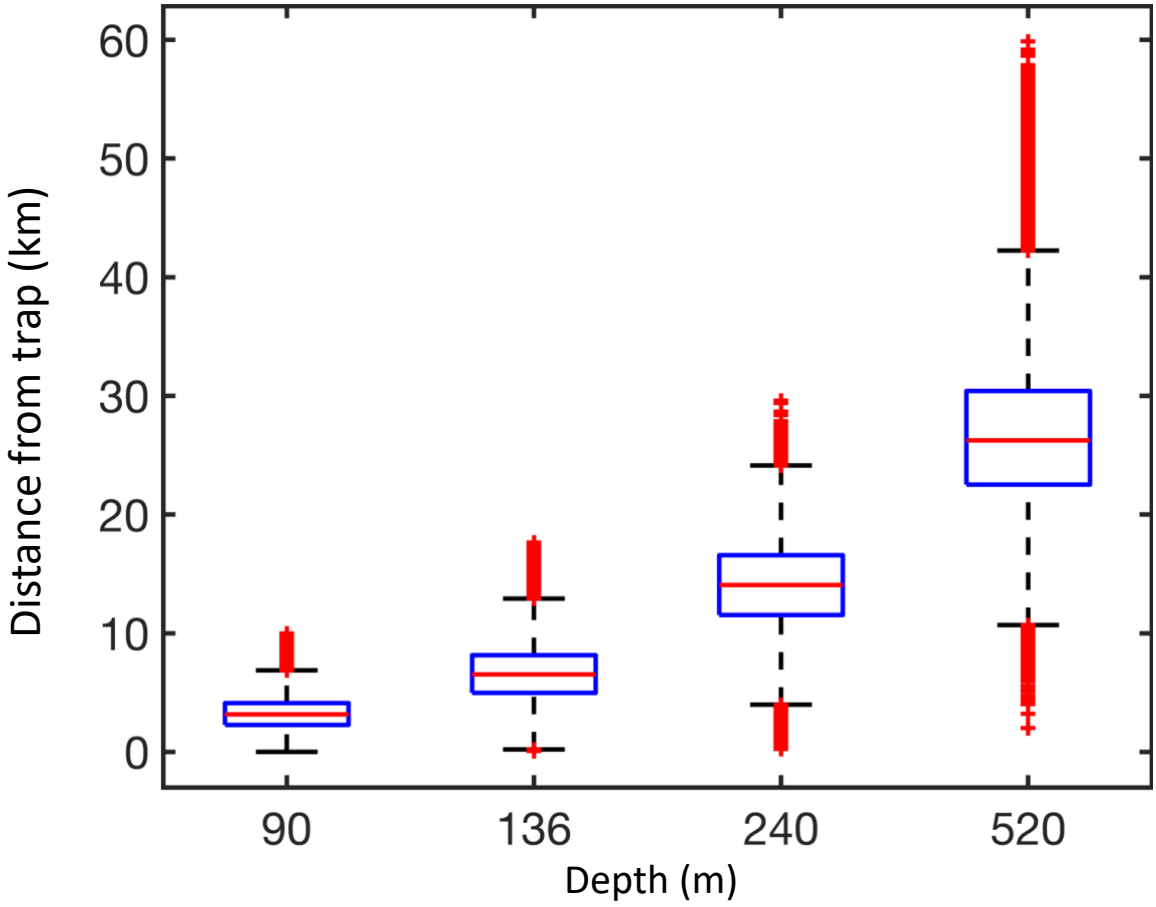

Figure 9 Horizontal distances of each point in the statistical funnel (position of the intercept of the particle's path with the base of the mixed layer) to the trap cup opening position at the time of capture for traps deployed to 90 m, 136 m, 240 m, and 520 m depth. The blue rectangles correspond to the interquartile range of the distribution of distances with respect to depth. The red line in the boxes corresponds to the median of the distribution of distances with respect to depth. The black bars in the extremity of the whiskers correspond to the statistical minimum and maximum values in the

distribution of distances with respect to depths excluding statistical outliers. The red crosses correspond to statistical outliers.

My analysis suggests that the shallowest traps and the deepest trap captured particles coming from different regions with minimal spatial overlap. In 95% of particle backtracking simulations (black whiskers in Figure 9), shallow traps captured particles that horizontally travelled less than 10 km, while particles captured by the deepest trap came from regions greater than 10 km from the deployment location. The distribution of distances for mid-water traps overlaps those for both the shallow and the deep traps.

Density plots

In Figure 10, the results for each statistical funnel are binned onto a 11 km latitude by 7 km longitude grid (corresponding to the grid from the chlorophyll satellite product). The percentage of points falling in each grid cell gives the probability for that grid cell to be the source of the observed POC flux at depth.

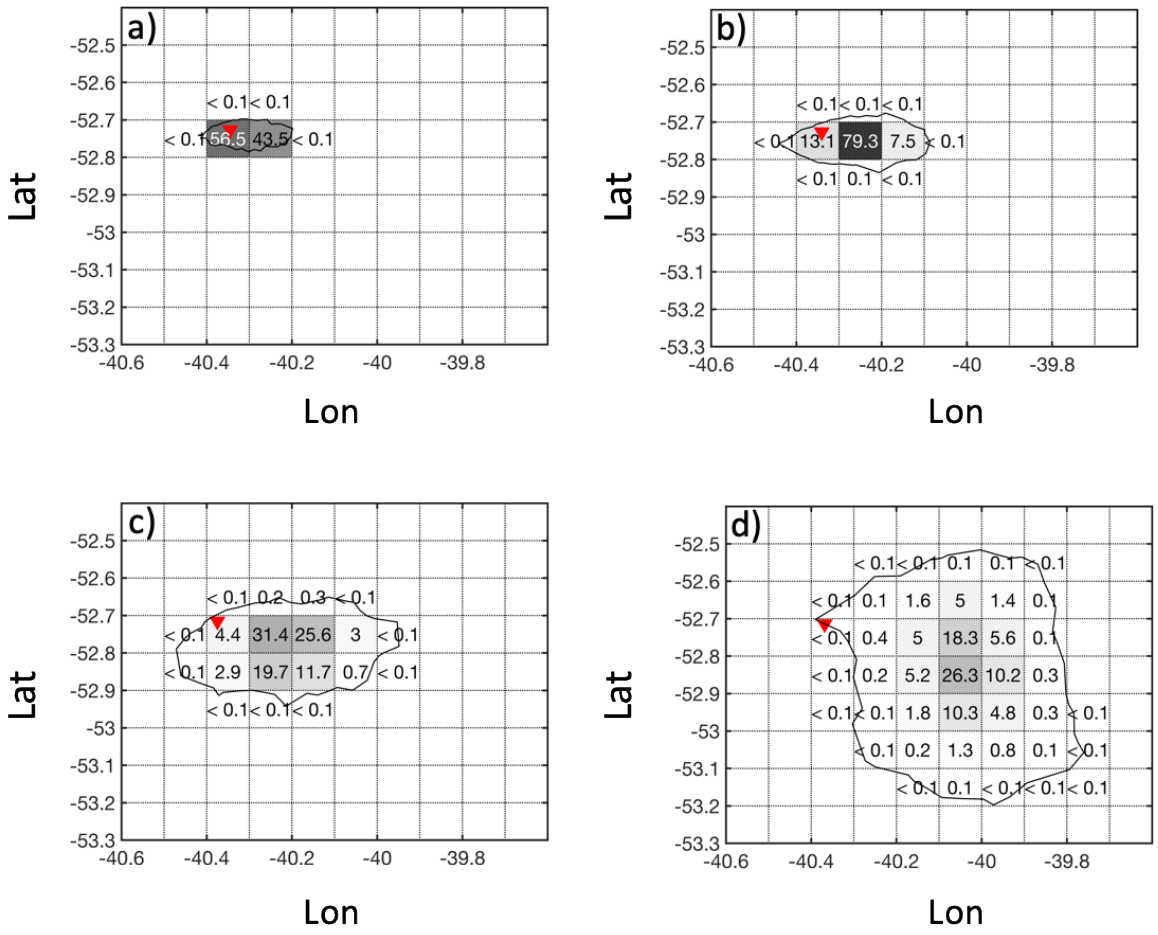

Figure 10 Probable POC flux source regions. Panels (a-d) present the results for the trap at 90 m, 136 m, 240 m and 520 m depth respectively. The black line is the envelope

enclosing all the points in the particle backtracking results (classic approach of a statistical funnel). The shaded squares represent the probability of that area to be the source region; the figures inside these squares are the probability that square is the source of the particles arriving at the trap.

The area of the source region "pancakes" (black outlines in Figure 10) increases with the sampling depth, while the intensity of the densest area decreases with the sampling depth (the sharpness of the results decreases with depth), suggesting an increase in uncertainty for the source region with depth. The trap at 90 m (Figure 9 a) sampled the region directly above the trap whereas the probability distribution for the 520 m trap (Figure 9 d) suggests that it sampled an area ~ 26 km to the southeast of its deployment location. The densest region drifted southeast between the two shallow traps and the deepest trap. This source drifting suggests particles captured deeper were exposed to a prevailing current coming from northwest of the site. This prevailing current might also have affected the two deepest traps, as they drifted northwest compared to the three shallow-most traps (see Figure 7).

Top:funnel–ratio

To assess the spatially induced bias introduced by the assumption that the flux comes straight down, I compared the chlorophyll concentration over the trap when the cup opened to the chlorophyll concentration at each point of my statistical funnel (denoted the top:funnel ratio). Figure 11 shows the distribution of these top:funnel ratios for all the points of the statistical funnels for each depth.

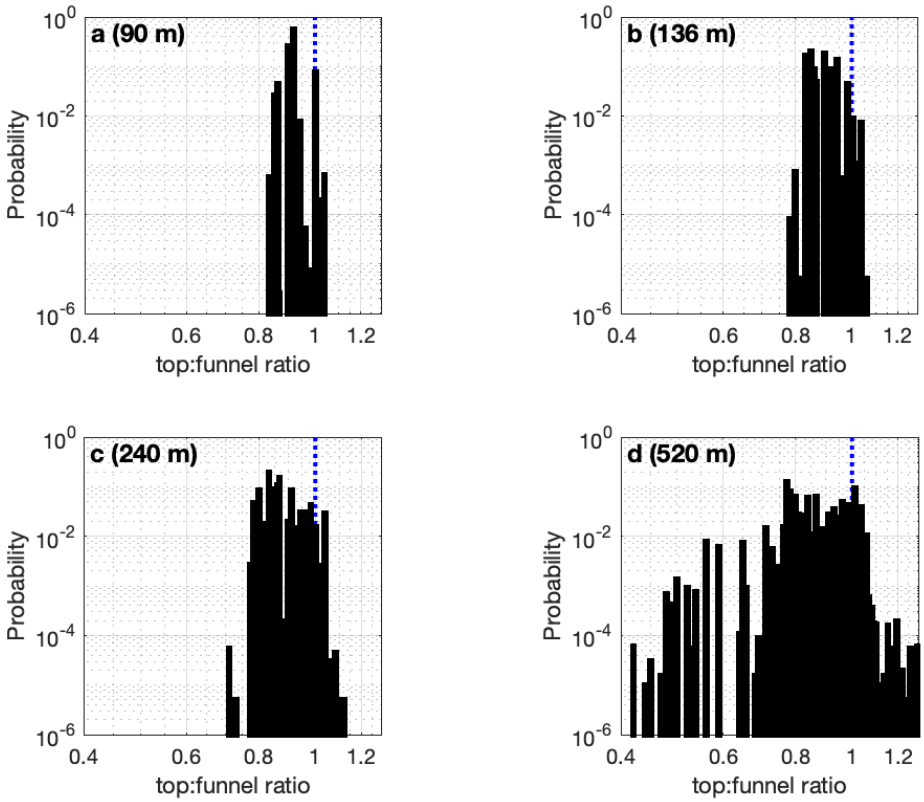

Figure 11 Histogram of the distribution of top:funnel chlorophyll ratios. Panels a-d present the results for the trap at 90 m, 136 m, 240 m, and 520 m depth. The blue dotted line represents a perfect match in chlorophyll concentration above the trap and at the source funnel. Note the log-scale in both axes.

Each of the 196006 runs of the Monte Carlo backtracking method produced a unique funnel position, corresponding to a unique funnel chlorophyll concentration and a unique top:funnel ratio, yielding a probability distribution of top:funnel ratio for each trap (Figure 11). Consistent with the increase in spread of the statistical funnel with depth (Figure 5), the spread in the top:funnel ratio also increases with depth. The deepest trap (Figure 11 d) had a bimodal distribution with a peak around 1 and a second peak lesser than one (around 0.8). The peak around 1 suggests the location intercepted by the statistical funnel could have had the same POC flux as directly over the trap (despite them being spatially distant). The second peak suggests the location intercepted by the statistical funnel had a greater POC flux than that directly above the trap. All the shallower traps had peaks in the probability distribution of < 1, suggesting that the POC flux was greater directly above the trap compared to the chlorophyll in the statistical funnel. Comparing the two deepest traps (Figure 11, panes c and d), we can see that the deepest trap has a larger top:funnel ratio range than the second deepest trap. This suggests that the deepest trap

could have sampled a region with a higher chlorophyll concentration than the second deepest trap.

Distribution of spatially adjusted b-values

To estimate the POC flux if particles had sunk directly downwards, the observed b-value is "spatially adjusted": the observed POC flux is multiplied by the top:funnel ratios found Figure 11. The b-value was then computed 2.9E21 times, each time drawing randomly from the probability distribution of spatially adjusted POC flux at each depth. Figure 12 is a histogram with all the resulting spatially adjusted b-values and their frequency.

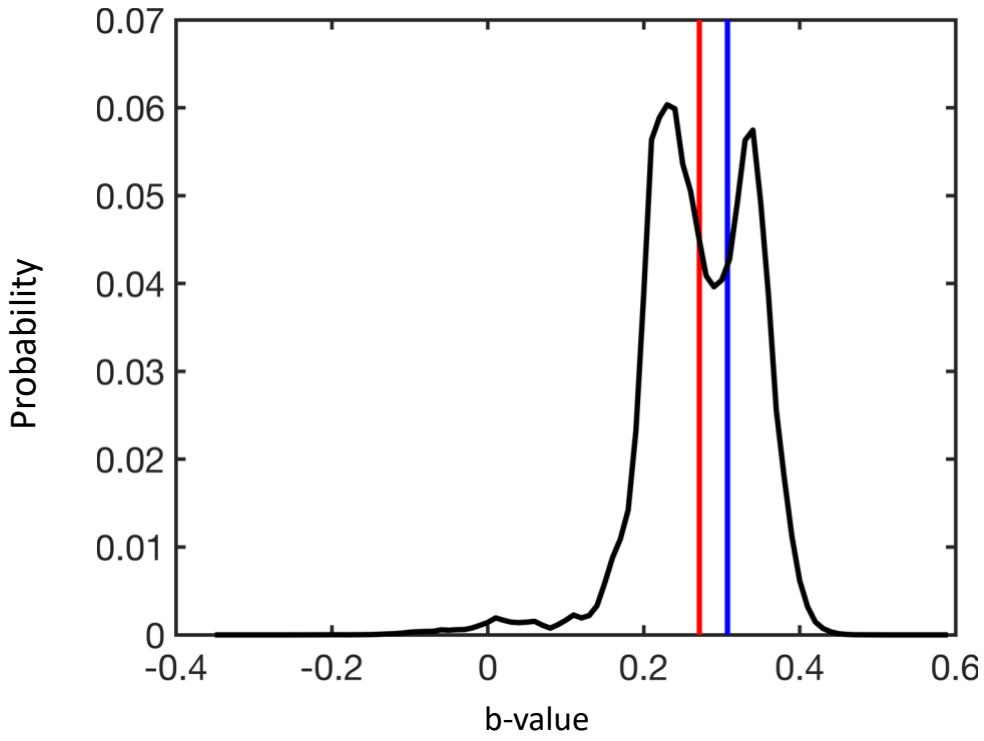

Figure 12 Probability distribution of spatially adjusted b-values (black curve). The mean and median of the distribution were 0.27 (red line) and the measured b-value was 0.31 (blue line). The 95 % interval centred on the mean of the distribution was [0.11; 0.38].

The spatially adjusted b-values follow a bimodal distribution with the peak probability for b at 0.23 and 0.34. The mean (and median) was 0.27. The observed b-value calculated directly from the data shown in Figure 8 (0.31) falls within the 95 % interval, and more specifically between the two peaks. The 95 % interval (from 0.11 to 0.38) suggests that spatial processes contributed to 25 % of the variability in the observed POC flux.

Discussion

My analysis of the relation between lateral advection and POC flux profiles observed using multiple simultaneous sediment trap deployments suggests that the traps at different depths might sample POC coming from distinct sources. Uncertainty in b arises from multiple sources when fitting the POC flux data to a Martin's curve. The study location had relatively low advection and therefore b-value estimates from flux profiles are expected to be robust. Nevertheless, surface chlorophyll fields suggest that POC flux observations are also spatially variable, when assuming chlorophyll is a proxy for POC. When looking at the deepest trap (P9 and P7, at 240 m and 520 m respectively), we can see that the flux measured by P7 is larger than the flux measured by P9 (see Figure 8). For each trap, we can look at the densest areas of the statistical funnel (Figure 10, panels c and d). The densest areas for both traps do not overlap. We can then investigate the chlorophyll values in the same area (Figure 6, right pane). The chlorophyll for P9 (the shallower trap) is lower than the one for P7. An explanation to the increased POC flux observation for P7, is that the trap sampled a region producing a higher POC flux than P9. Nevertheless, this does not exclude other possible sources of errors, such as analytical error, that could be a significant source of error for such fluxes. The results in Figure 11 suggest that, at all depths, assuming a purely vertical flux of POC to depth would underestimate the flux attenuation as the deepest trap likely sampled a region capable of generating a larger POC flux than its immediately shallower counterpart. This decreases the perceived attenuation at depth. If the deepest trap would have had a source generating a similar POC flux as its shallower counterpart, the deepest trap would have had a lower POC flux observation (assuming the flux attenuation is constant in the region). See Figure 13 for a summary of the data used in this part of the discussion.

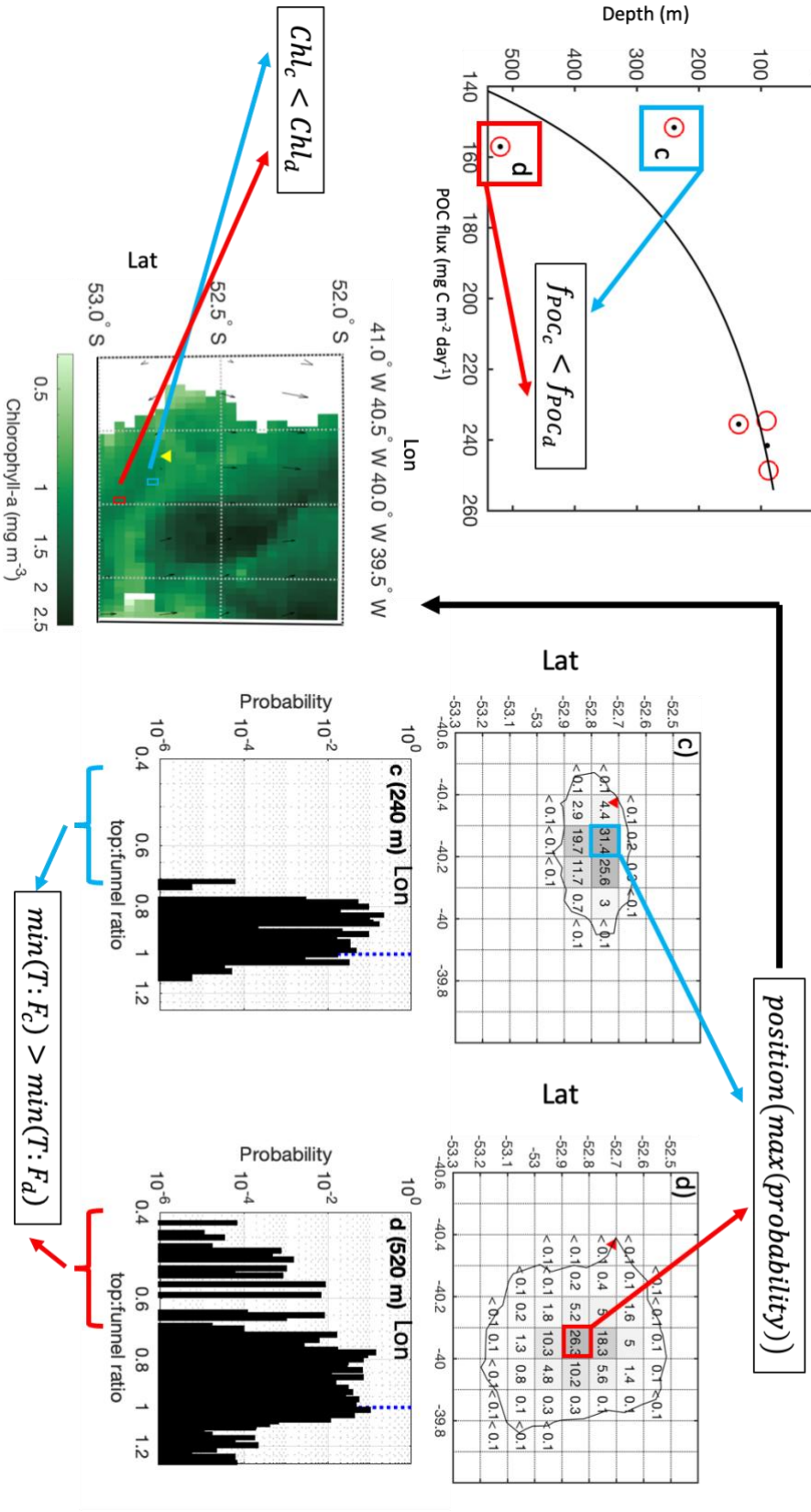

Figure 13 Summary figure presenting the approach of the analysis comparing the two deepest traps (denoted c and d). This composite figure is an adaptation of Figure 6, Figure 8, Figure 10, and Figure 11. Blue lines correspond to the trap c and red corresponds to trap d.

I found that advection could contribute up to 25 % of the uncertainty in b when using the raw POC flux data from the traps. Patchiness in the surface chlorophyll is a contributing factor to the uncertainty added by lateral advection in b. Other, more advective regions, may well have higher contributions of advection to uncertainty in b.

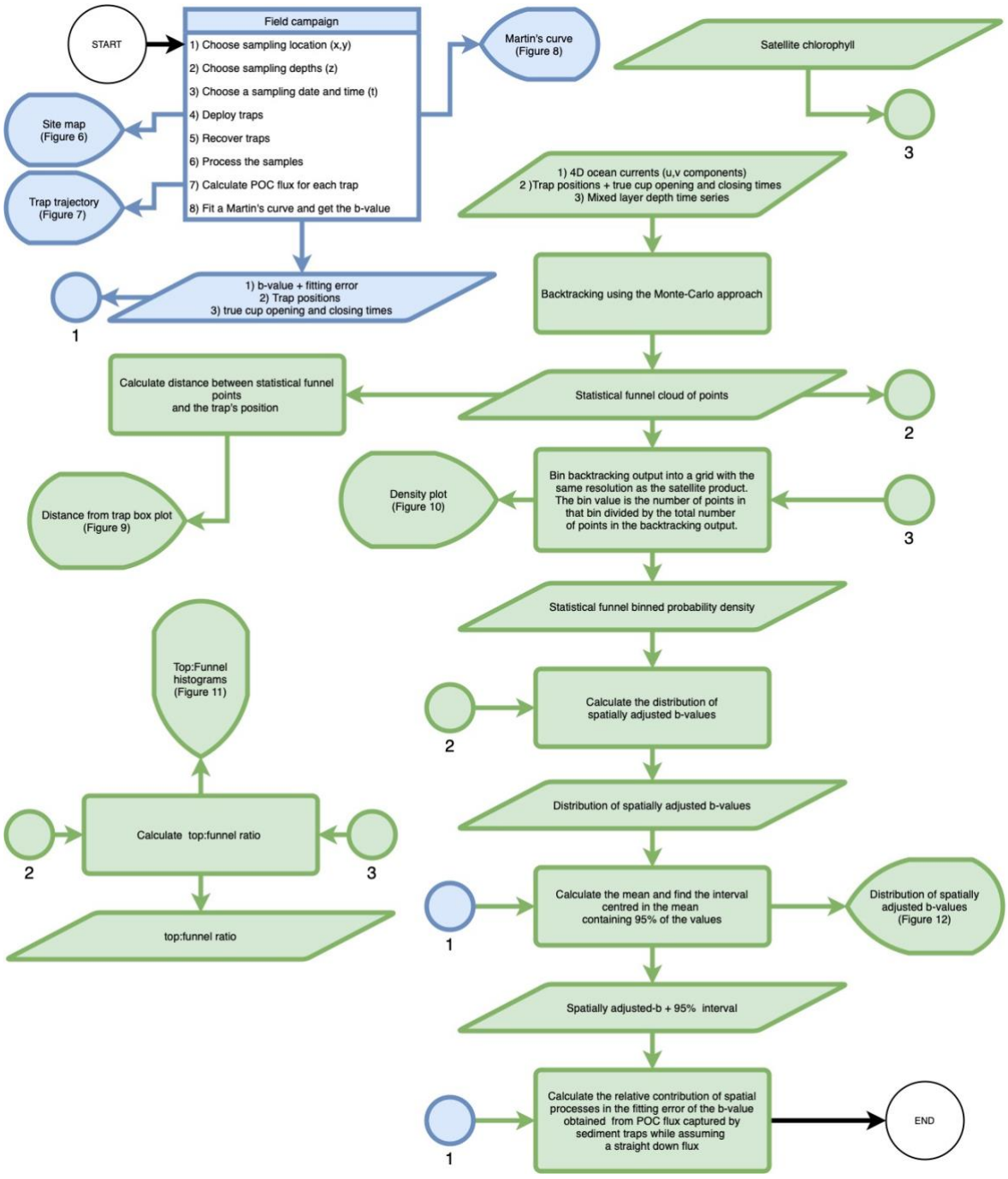

Figure 14 Summary of the method. The blue path is the workflow that is currently used by the community. The green path is my suggested method to complement the current workflow. Parallelograms represent loading/saving data, rectangles are processes, circles are in page references and balloons are graphical outputs. Arrows represent

processes inputs/outputs. They also correspond to the processes flow. The white circles correspond to the starting and ending point of the flowchart.

The method I propose better constrains the statistical funnel geographical region (compared to Siegel and Deuser (1997)). Additionally, my method suggests a probability density map, which takes into consideration errors in ocean currents. My method stops the backtracking at the base of the mixed layer, allowing to account for changes in the mixed layer (for instance, if the mixed layer depth is increasing with time, the depth for the POC flux source for the deepest trap will be shallower than the source depth of more shallow traps), this ensures that the backtracking is not performed inside the mixed layer. My method also uses 4D horizontal currents, opposed to sea surface currents in Siegel and Deuser (1997) and Espinola (2018). By normalizing the source region by the pixel above the traps (top:funnel ratio), we can better understand the role of spatial variability in POC flux error. The top:funnel ratio can be used to indicate what bias is introduced with the flux straight down assumption. Studying top:funnel ratios, density plots and the surface chlorophyll field can provide us with insights on observational POC flux profiles. Giering et al. (2017) challenges the steady state assumption, showing that the timing of the phytoplankton bloom and the timing of field campaign can impact observations. My study can be used together with Giering et al. (2017) to account for spatial-temporal influences in POC flux errors. Finally, my study suggests a method to calculate a distribution of spatially normalized b-values. This is the equivalent of removing the effect of spatial variability in the POC flux profile. See Figure 14 for a summary of my method.

Limitations of the approach

All the assumptions and limitations presented here were necessary to perform the analysis. Some of the limitations were due to limits in the computing power, while others were due to unknowns in the field.

The ocean currents used in our analysis come from an assimilative global model and comprised daily means of zonal and meridional velocities, with no vertical velocity component. I do not have in situ observations to verify the performance of the model during the time taken for a particle to sink from the mixed layer to the sediment traps. The assumed absence of vertical velocities could introduce a bias in the sinking particle time scale and intercept with the base of the mixed layer. However, at this study site, sustained vertical velocities are expected to be negligible relative to sinking speed of 50 m d^{-1}, even though instantaneous vertical velocities can be higher.

Consequently, the absence of vertical velocities in the modelled currents is assumed to have little effect on the source location of the particles.

In my method I used chlorophyll as a linear proxy for the POC flux. In practice, while a positive relationship is expected, the relationship may well be non-linear (Legendre 1999). Additionally, there is likely a lag between changes in surface chlorophyll concentration and POC flux, which has not been taken into account in this study (Henson et al. 2015). Using the chlorophyll-a to POC relation suggested in Legendre (1999) $POC = 2.27 + 0.35 \cdot \log(chl)$ for depths ≤ 300 m and $POC = 2.16 + 0.61 * \log(chl)$ for depths > 300 m, the distribution shown in Figure 11 would deviate further from 1, i.e. uncertainty in b would increase. However, the relationships proposed in Legendre (1999) are not site specific and have respective R^2 of 0.40 and 0.65. They therefore do not fully explain the relationship between chlorophyll and POC.

Particles were assumed to be created solely within the mixed layer and to have a constant sinking speed. However, there is evidence that particles can be created and/or modified throughout the water column, e.g. through fragmentation (Boyd and Stevens 2002). Particles can also be introduced at depth by other facets of the BCP, such as subduction (Boyd et al. 2019). Sinking speed is also not likely to be constant over time (Berelson 2001; Omand et al. 2020). Our model does not capture these particle dynamics.

Variability introduced by temporal processes such as defined by Giering et al. (2017) were not taken into consideration in our approach. Any remaining variability comes from other processes (such as particle dynamics).

Limitations of the case study

Because of the predominance of clouds in our study region, only a single, relatively clear satellite chlorophyll image was available. The dynamics of the chlorophyll over time are therefore not taken into consideration here. Additionally, there are technical limitations in satellite observations that could introduce variability. These are artefacts present in satellite chlorophyll products (e.g., banding effect, icebergs, and clouds). Our source locations are near the edges of an area of banding in the satellite image, which might introduce additional variability in our results.

I assumed that the free-drifting sediment traps behaved as perfect Lagrangian drifters at a constant depth. In practice sediment trap design can have an influence on the captured flux, introducing a bias in the POC flux sampling (Baker et al. 2020). The drift depths of the sediment traps are also not constant, as they oscillate around their target depth (see Table 1). These oscillations can be an additional source of error for both POC flux measurements and for our

model. The trap position when the collection cups are opened and closed was estimated by a linear interpolation between the deployment location and re-surfacing location. The real path of the trap is unknown, but it is unlikely that it was entirely linear.

Implications of the case study results

A first indication that the assumption of purely vertically sinking flux may be in error comes from the increase in POC flux observed in our deepest trap. POC flux is not expected to increase with depth as it is expected to be respired as it sinks, which, at steady state, implies a decrease of the flux with depth. The observed increase with depth could be explained either by an under-trapping issue for the 240 m deep trap, an in situ mid-depth source of sinking POC, or by a different flux source and intensity between these two traps. Our results imply that the latter explanation is the most likely in this case.

At a site where the magnitude of surface currents is low (such as this), the assumption that the POC flux sinks purely vertically might be used to simplify the flux profile interpretation. However, surface currents do not necessarily reflect the behaviour of the currents at depth. The surfacing position of the traps (Figure 7) is a tangible example showing surface currents are not a good proxy for the currents in the water column. The traps emerged in two distinct groups which followed a different mean direction throughout their deployment. It is worth noting the traps had been exposed to the currents for a short period of time (24 hours) relative to the sinking flux time scale (~ 8 d to reach the deepest trap with a sinking speed of 50 m d^{-1}).

Additionally, the assumption that the flux sank purely vertically into the trap does not seem to hold as the region sampled by the deeper traps was over 10 km away from the trap location. The deeper traps therefore likely sampled different chlorophyll patches within the mixed layer than the shallower traps, thus contributing to the variability in our observed POC flux profile.

Our results suggest that applying the vertical flux assumption to the data collected during this cruise would likely have overestimated the POC flux at depth. For our site near South Georgia, spatial variability contributed about 25% to uncertainty in the b-value. Other more dynamic regions are likely to experience larger uncertainties in b introduced by spatial variability.

The results presented here are specific to our site, and more precisely to our deployment. Lampitt et al (in preparation) conducted a similar study using the same backtracking method applied to the Porcupine Abyssal Plain (PAP) site in the Northeast Atlantic which concluded that spatial variability is not a major contributor to variability in observed flux in their deepest sediment trap

(3000 m). However, the chlorophyll-a field was less variable and regional surface currents were slower and less variable at the PAP site compared to our site.

The contrasting results between our study and the PAP site highlight the need to perform site-specific statistical funnel studies to facilitate the choice of sampling strategy.

POC observations at depth are a composite of particles with different sinking speeds, and therefore sources. This diversity in sources needs to be further studied to fully understand the true impact of spatial processes in observed flux profiles, and consequently in the b-value. Additionally, even if the top:funnel ratio is 1 and there is no bias in b, there might be other important differences in the POC flux composition.

Conclusions

Our study found that despite being in a relatively low advection site, spatial variability contributed up to 25 % of the uncertainty in b; however, this result is valid only for Station P3 (52.7 °S, 48.1 °W) during COMICS I (November-December 2017). Other more advective regions could potentially have an even larger contribution of spatial variability to the uncertainty in b. The approach used here could be used to improve the understanding of POC flux profiles, especially in highly advective sites such as Eastern Boundary upwelling zones.

Future work

The method proposed here can be used for assessing the role of spatial variability in the uncertainty in the b-value. This method can also be used for the planning of field campaigns, by providing insights on particle trajectory dynamics and how spatial variability in the surface layer could influence observations at depth. Additionally, the method incentivises the use of in situ current observations to better understand the BCP.

One of the key limitations in this method is sinking speed and sinking speed dynamics. The method assumes a constant bulk sinking speed. A sensitivity analysis could be made by repeating the method in the same site and starting points using different sinking speeds. Additionally, sinking speeds are considered constant in time and depth in the method. A probability-based approach could enhance the model by introducing variable sinking speeds. To do so, two more parameters are needed: the probability to have a change in the sinking speed. Density (salinity and heat) exchanges with the environment can also be added to the model, where an increase in salinity or a decrease in temperature result in an increase in particle density and therefore an increase in sinking speed.

Another aspect that would benefit from further study is the impact of particle transformation on the results of the statistical funnel. This includes processes such as aggregation/disaggregation, repackaging (with an increase or decrease in density), entrainment, detrainment, and biologically mediated transportation. A key process that could be also included is respiration. Adding respiration would allow us to better understand the pathways of the BCP-related CO_2 in and out of the ocean.

This method is highly dependent on modelled current velocity. The method could benefit from using observational data for sub-surface currents that include a vertical component. An ADCP could be deployed in the study site prior to the deployment of BCP observational tools (such as sediment traps) to collect sub-surface current data to be used instead of model data. Autonomous platforms could also provide us with observational insights on the mixed layer depth. These autonomous platforms could also provide us with observational data to validate our method. This could be done by comparing our particle trajectories with data from autonomous platform whose path cross the particle's trajectories, looking for overlaps in the signal.

Finally, this study could be repeated in other sites to better understand the variability in b introduced by spatial variability and what are the key factors contributing to the variability in b.

Glossary of Terms

BCP..... Biological carbon pump: atmospheric carbon removal by the ocean's biology.

DIC..... Dissolved inorganic carbon: aqueous inorganic carbon in the ocean

NOC..... National Oceanography Centre

PELAGRA ..... Particle Export measurement using a Lagrangian trap: a drifting autonomous sediment trap used to collect and/or observe particulate organic carbon flux at a target depth and time.

PAP..... Porcupine Abyssal Plain: long-term study site located in the Northeast Atlantic Ocean at 49.0°N 016.5°W with a depth of 4850 m.

POC ..... Particulate organic carbon: fraction of the organic carbon with a size ranging from 53 µm to 2 mm.

List of References

Baker, C. A., M. L. Estapa, M. Iversen, R. Lampitt, and K. Buesseler. 2020. Are all sediment traps created equal? An intercomparison study of carbon export methodologies at the PAP-SO site. Progress in Oceanography **184**.

Berelson, W. M. 2001. Particle settling rates increase with depth in the ocean. Deep Sea Research Part II: Topical Studies in Oceanography **49:** 237-251.

Boyd, P. W., H. Claustre, M. Levy, D. A. Siegel, and T. Weber. 2019. Multi-faceted particle pumps drive carbon sequestration in the ocean. Nature **568:** 327-335.

Boyd, P. W., and C. L. Stevens. 2002. Modelling particle transformations and the downward organic carbon flux in the NE Atlantic Ocean. Progress in Oceanography **52:** 1-29.

Briggs, N., G. Dall'Olmo, and H. Claustre. 2020. Major role of particle fragmentation in regulating biological sequestration of CO2 by the oceans. Science **367:** 791-793.

Buesseler, K. O., and P. W. Boyd. 2009. Shedding light on processes that control particle export and flux attenuation in the twilight zone of the open ocean. Limnology and Oceanography **54:** 1210-1232.

Burd, A. B., and G. A. Jackson. 2009. Particle aggregation. Ann Rev Mar Sci **1:** 65-90.

Cael, B. B., and K. Bisson. 2018. Particle Flux Parameterizations: Quantitative and Mechanistic Similarities and Differences. Frontiers in Marine Science **5**.

Cavan, E. L., S. A. Henson, A. Belcher, and R. Sanders. 2017. Role of zooplankton in determining the efficiency of the biological carbon pump. Biogeosciences **14:** 177-186.

Deuser, W. G., F. E. Muller-Karger, and C. Hemleben. 1988. Temporal variations of particle fluxes in the deep subtropical and tropical North Atlantic: Eulerian versus Lagrangian effects. Journal of Geophysical Research **93**.

East, H. 2019. Contribution of slow versus fast sinking particles during the high latitude South Atlantic spring bloom Original typescript. University of Southampton.

Espinola, B. 2018. Neutrally buoyant sediment traps collect particles from further away than previously considered. University of Southampton.

Fowler, S. W., and G. A. Knauer. 1986. Role of large particles in the transport of elements and organic compounds through the oceanic water column. Progress in Oceanography **16:** 147-194.

Friedlingstein, P. and others 2019. Global Carbon Budget 2019. Earth System Science Data **11:** 1783-1838.

Giering, S. L. C., and M. P. Humphreys. 2017. Biological Pump, p. 1-6. *In* W. M. White [ed.], Encyclopedia of Engineering Geology. Encyclopedia of Earth Sciences Series. Springer International Publishing.

Giering, S. L. C. and others 2017. Particle flux in the oceans: Challenging the steady state assumption. Global Biogeochem Cy **31:** 159-171.

Gruber, N. and others 2019. The oceanic sink for anthropogenic CO2 from 1994 to 2007. Science **363:** 1193-1199.

Henson, S. A., C. Laufkötter, S. Leung, S. L. C. Giering, H. I. Palevsky, and E. L. Cavan. 2022. Uncertain response of ocean biological carbon export in a changing world. Nature Geoscience **15:** 248-254.

Henson, S. A., R. Sanders, E. Madsen, P. J. Morris, F. Le Moigne, and G. D. Quartly. 2011. A reduced estimate of the strength of the ocean's biological carbon pump. Geophysical Research Letters **38:** L04606.

Henson, S. A., A. Yool, and R. Sanders. 2015. Variability in efficiency of particulate organic carbon export: A model study. Global Biogeochem Cy **29:** 33-45.

Herndl, G. J., and T. Reinthaler. 2013. Microbial control of the dark end of the biological pump. Nat Geosci **6:** 718-724.

Humphreys, M. P., E. R. Lewis, J. D. Sharp, and D. Pierrot. 2022. PyCO2SYS v1.8: marine carbonate system calculations in Python. Geoscientific Model Development **15:** 15-43.

Korb, R. E., M. J. Whitehouse, A. Atkinson, and S. E. Thorpe. 2008. Magnitude and maintenance of the phytoplankton bloom at South Georgia: a naturally iron-replete environment. Marine Ecology Progress Series **368:** 75-91.

Kwon, E. Y., F. Primeau, and J. L. Sarmiento. 2009. The impact of remineralization depth on the air–sea carbon balance. Nature Geoscience **2:** 630-635.

Lampitt, R. S. and others 2008a. Ocean fertilization: a potential means of geoengineering? Philos Trans A Math Phys Eng Sci **366:** 3919-3945.

Lampitt, R. S. and others 2008b. Particle export from the euphotic zone: Estimates using a novel drifting sediment trap, 234Th and new production. Deep Sea Research Part I: Oceanographic Research Papers **55:** 1484-1502.

Lampitt, R. S., T. Noji, and B. von Bodungen. 1990. What happens to zooplankton faecal pellets? Implications for material flux. Marine Biology **104:** 15-23.

Landschützer, P., T. Ilyina, and N. S. Lovenduski. 2019. Detecting Regional Modes of Variability in Observation-Based Surface Ocean pCO2. Geophysical Research Letters **46:** 2670-2679.

Laruelle, G. G., R. Lauerwald, B. Pfeil, and P. Regnier. 2014. Regionalized global budget of the CO2exchange at the air-water interface in continental shelf seas. Global Biogeochem Cy **28:** 1199-1214.

Legendre, L. 1999. Chlorophyll a to estimate the particulate organic carbon available as food to large zooplankton in the euphotic zone of oceans. Journal of Plankton Research **21:** 2067-2083.

Martin, J. H., G. A. Knauer, D. M. Karl, and W. W. Broenkow. 1987. VERTEX: carbon cycling in the northeast Pacific. Deep Sea Research Part A. Oceanographic Research Papers **34:** 267-285.

Meredith, M. P. 2003. Southern ACC Front to the northeast of South Georgia: Pathways, characteristics, and fluxes. Journal of Geophysical Research **108**.

Omand, M. M., R. Govindarajan, J. He, and A. Mahadevan. 2020. Sinking flux of particulate organic matter in the oceans: Sensitivity to particle characteristics. Sci Rep **10:** 5582.

Parekh, P., S. Dutkiewicz, M. J. Follows, and T. Ito. 2006. Atmospheric carbon dioxide in a less dusty world. Geophysical Research Letters **33:** L03610.

Passow, U., and C. A. Carlson. 2012. The biological pump in a high CO2 world. Marine Ecology Progress Series **470:** 249-271.

Robinson, C. and others 2010. Mesopelagic zone ecology and biogeochemistry – a synthesis. Deep Sea Research Part II: Topical Studies in Oceanography **57:** 1504-1518.

Roobaert, A., G. G. Laruelle, P. Landschützer, N. Gruber, L. Chou, and P. Regnier. 2019. The Spatiotemporal Dynamics of the Sources and Sinks of CO2 in the Global Coastal Ocean. Global Biogeochem Cy **33:** 1693-1714.

Sanders, R. J. and others 2016. Controls over Ocean Mesopelagic Interior Carbon Storage (COMICS): Fieldwork, Synthesis, and Modeling Efforts. Frontiers in Marine Science **3**.

Shadwick, E. H., H. Thomas, A. Comeau, S. E. Craig, C. W. Hunt, and J. E. Salisbury. 2010. Air-Sea CO₂ fluxes on the Scotian Shelf: seasonal to multi-annual variability. Biogeosciences **7:** 3851-3867.

Siegel, D. A., and W. G. Deuser. 1997. Trajectories of sinking particles in the Sargasso Sea: modeling of statistical funnels above deep-ocean sediment traps. Deep Sea Research Part I: Oceanographic Research Papers **44:** 1519-1541.

Siegel, D. A., E. Fields, and K. O. Buesseler. 2008. A bottom-up view of the biological pump: Modeling source funnels above ocean sediment traps. Deep Sea Research Part I: Oceanographic Research Papers **55:** 108-127.

Siegel, D. A., T. C. Granata, A. F. Michaels, and T. D. Dickey. 1990. Mesoscale eddy diffusion, particle sinking, and the interpretation of sediment trap data. Journal of Geophysical Research **95**.

Smith, K. M., P. E. Hamlington, K. E. Niemeyer, B. Fox-Kemper, and N. S. Lovenduski. 2018. Effects of Langmuir Turbulence on Upper Ocean Carbonate Chemistry. Journal of Advances in Modeling Earth Systems.

Thorpe, S. E., K. J. Heywood, M. A. Brandon, and D. P. Stevens. 2002. Variability of the southern Antarctic Circumpolar Current front north of South Georgia. Journal of Marine Systems **37:** 87-105.

Tranvik, L. J. and others 2009. Lakes and reservoirs as regulators of carbon cycling and climate. Limnology and Oceanography **54:** 2298-2314.

Waniek, J., W. Koeve, and R. D. Prien. 2000. Trajectories of sinking particles and the catchment areas above sediment traps in the northeast Atlantic. Journal of Marine Research **58:** 983-1006.

Wanninkhof, R. and others 2013. Global ocean carbon uptake: magnitude, variability and trends. Biogeosciences **10:** 1983-2000.

Watson, A. J. and others 2009. Tracking the variable North Atlantic sink for atmospheric CO2. Science **326:** 1391-1393.

Woolf, D. K., P. E. Land, J. D. Shutler, L. M. Goddijn-Murphy, and C. J. Donlon. 2016. On the calculation of air-sea fluxes of CO2in the presence of temperature and salinity gradients. J Geophys Res-Oceans **121:** 1229-1248.